2018

Mechanical response and pore pressure generation in granular filters subjected to uniaxial cyclic loading

Jahanzaib Israr
University of Wollongong, jisrar@uow.edu.au

Buddhima Indraratna
University of Wollongong, indra@uow.edu.au

Mechanical response and pore pressure generation in granular filters subjected to uniaxial cyclic loading

Abstract

This paper presents results from a series of piping tests carried out on a selected range of granular filters under static and cyclic loading conditions. The mechanical response of filters subjected to cyclic loading could be characterized in three distinct phases; namely, (I) pre-shakedown, (II) post-shakedown, and (III) post-critical (i.e., the occurrence of internal erosion). All the permanent geomechanical changes such, as erosion, permeability variations, and axial strain developments, took place during phases I and III, while the specimen response remained purely elastic during phase II. The post-critical occurrence of erosion incurred significant settlement that may not be tolerable for high-speed railway substructures. The analysis revealed that a cyclic load would induce excess pore-water pressure, which, in corroboration with steady seepage forces and agitation due to dynamic loading, could then cause internal erosion of fines from the specimens. The resulting excess pore pressure is a direct function of the axial strain due to cyclic densification, as well as the loading frequency and reduction in permeability. A model based on strain energy is proposed to quantify the excess pore-water pressure, and subsequently validated using current and existing test results from published studies.

Disciplines

Engineering | Science and Technology Studies

Publication Details

Israr, J. & Indraratna, B. (2018). Mechanical response and pore pressure generation in granular filters subjected to uniaxial cyclic loading. Canadian Geotechnical Journal, 55 (12), 1756-1768.

Mechanical Response and Pore Pressure Generation in Granular Filters subjected to Uniaxial Cyclic Loading

Jahanzaib Israr, BSc (Pak), MSc (Lhr.), PhD (Wollongong)
Associate Research Fellow, Centre for Geomechanics and Railway Engineering (GRE), Faculty of Engineering, Univ. of Wollongong, Wollongong City, NSW 2522, Australia. Assistant Professor of Civil Engineering, Univ. of Engineering and Technology Lahore, Pakistan (On study leave). E-mail: jisrar@uow.edu.au

Buddhima Indraratna, BSc (Eng), MSc (Lond.), DIC, PhD (Alberta), FIEAust., FASCE
Distinguished Professor of Civil Engineering, Founding Director of Centre for Geomechanics and Railway Engineering (GRE), Faculty of Engineering, Faculty of Engineering, Univ. of Wollongong, Wollongong City, NSW 2522, Australia. E-mail: indra@uow.edu.au

Date of Submission: 06 November 2017

Submitted to: Canadian Geotechnical Journal

Author for correspondence:
Dr. J. Israr
Faculty of Engineering
University of Wollongong
Wollongong, NSW 2522
Australia.
Ph: +61 2 4221 3046
Fax: +61 2 4221 3238
Email: jisrar@uow.edu.au

Mechanical Response and Pore Pressure Generation in Granular Filters subjected to Uniaxial Cyclic Loading

Jahanzaib Israr, Ph.D[1] and Buddhima Indraratna, Ph.D., F.ASCE[2]

Abstract:

This paper presents the results from a series of piping tests carried out on a selected range of granular filters under static and cyclic loading conditions. The mechanical response of filters subjected to cyclic loading could be characterised in 3 distinct phases; namely (i) pre-shakedown, (II) post-shakedown, and (III) post-critical (i.e. the occurrence of internal erosion). All the permanent geomechanical changes such as erosion, permeability variations and axial strain developments took place during phases I and III, while the specimen response remained purely elastic during phase II. The post-critical occurrence of erosion incurred significant settlement that may not be tolerable for high-speed railway substructures. The analysis revealed that a cyclic load would induce excess pore water pressure, which, in corroboration with steady seepage forces and agitation due to dynamic loading could then cause internal erosion of fines from the specimens. The resulting excess pore pressure is a direct function of the axial strain due to cyclic densification, as well as the loading frequency and reduction in permeability. A model based on strain energy is proposed to quantify the excess pore water pressure, and subsequently validated using current and existing test results from published studies.

Author keywords: Granular filters, Pore pressure, Internal erosion, Cyclic load, Frequency

==========

[1]Associate Research Fellow, Centre for Geomechanics and Railway Engineering (GRE), Faculty of Engineering, Univ. of Wollongong, Wollongong City, NSW 2522, Australia. Assistant Professor of Civil Engineering, Univ. of Engineering and Technology Lahore, Pakistan. (corresponding author). E-mail: jisrar@uow.edu.au.

[2]Distinguished Professor of Civil Engineering, Founding Director Centre GRE, Faculty of Engineering, Univ. of Wollongong, Wollongong City, NSW 2522, Australia. E-mail: indra@uow.edu.au.

Introduction

Granular filters protect base soils such as dam cores and natural erodible subgrades from erosion, while alleviating potential build-up of excess pore water pressure. Recent advances in geotechnical practices have generated an interest in applying these granular filters to geohydraulic and transportation infrastructure facilities (Sansalone et al. 2008; Koerner et al. 1994; Fourie et al. 1994), where filtration occurs under adverse loading conditions (i.e. both static and cyclic loading). Unlike large upstream seepage heads in dams, hydraulic excitation in railway sub-structures stems mainly from the generation of pore water pressure in natural subgrades and engineered fills, e.g. subballast (Indraratna et al. 2017; Selig and Waters 1994). Previous studies revealed that the filters within these structures would be under complex dynamic stress states and thus have a significant influence on the erosion of fine particles such as base-soil migration, suffusion, and internal erosion (Indraratna et al. 2017; Chang and Zhang 2013; Xiao and Shwiyhat 2012; Trani and Indraratna 2010; Burenkova 1993). Nonetheless, limited migration of base fines into filters may occasionally establish self-filtering layers that help prevent any further erosion and increase their internal stability. However, strong upward seepage may develop significant structural instabilities such as piping, segregation erosion and heave, and associated deterioration in permeability as base soil erodes into the overlying filter layers may initiate progressive clogging, especially under cyclic loading conditions (Trani and Indraratna 2010).

The loading conditions in railway substructures are cyclic, unlike the steady seepage under static loading that usually occurs in dams and levees. A subballast filter performs two major functions in track environments; namely (a) cope with the sustainable transfer of stress from the ballast to the subgrade, and (b) protect subgrade fines from upward pumping due to seepage and the build-up of pore pressure due to cyclic loading. An effective subballast filter mitigates ballast fouling from the substructure and reduces the risk of track settlement and related

instability due to clay pumping (Selig and Waters 1994). However, inadequately designed subballast subjected to excessive pore pressure and agitation induced by cyclic loading could lose its own finer fractions to internal erosion, and thereby experience changes in its particle gradation (i.e. internal instability) which may result in a highly porous and ineffective filter layer.

As Figure 1 shows, cyclic loading induces significant magnitude of pore water pressure (Δu), which may be classified into two components, namely: residual and transient (Sassa and Sekiguchi 1999). Given that the mean of transient Δu is usually zero, it does not accumulate and thus causes no significant reductions in the effective stresses of soils. However, the residual component of Δu may accumulate over time at higher loading frequencies, depending on the soil properties, the volumetric strain rate, drainage conditions, and the number of loading cycles (Trani and Indraratna 2010; Polito et al. 2008). A large increase in the accumulated residual Δu may disturb the constriction size distribution (CSD) network quite considerably and reduce the effective stress in soils (Indraratna et al. 2017; Xiao et al. 2006). The possible results of this Δu generation may include but not be limited to excessive internal erosion, premature suffusion and piping in the drainage layer, as well as fluidization of soft saturated natural subgrades, thus causing the substructure to experience severe mud-pumping and excessive ballast fouling from the substructure (Indraratna et al. 2012; Selig and Waters 1994).

Thus far, various researchers have attempted to model the generation of pore pressure in granular soils to quantify their potential for liquefaction during earthquakes. The existing models of pore pressure generation are either (a) stress based, or (b) energy based. The former are generally built empirically based on laboratory and field observations which have been continually refined through novel studies and classical case histories (e.g. Seed and Idris 1971; Youd et al. 2001). In contrast, the energy based models use relationships between various forms of energy released during seismic activities and the corresponding pore water pressure (e.g.

Gutenberg and Richter 1942; Nemat-Nasser and Shokooh 1979). Given that the period and number of cycles of high-speed train loading are generally greater than the dynamic load during a typical earthquake, the likelihood of significant pore pressure developing in railway substructures can be very high. The authors realise that there is no specific and elaborate literature on the generation of pore pressure in railway substructures, so this current study purports to improve our understanding of this phenomenon and attempts to model the development of pore water pressure in subballast filters subjected to high-speed cyclic loading. In this regard, a series of hydraulic tests under static and cyclic loading conditions was carried out on a selected range of compacted granular soils. An analysis of the static and cyclic tests is presented and a semi-empirical energy based approach is proposed herein to capture the generation of pore pressure in granular filters subjected to cyclic train loading.

In this study, a total of 32 hydraulic tests have been carried out in two different phases. In first phase, 16 hydraulic tests were conducted under static loading with a twofold objective; namely (1) to examine the effects of overburden confinement to simulate stationary train conditions on the mechanical and drainage characteristics of subballast filters, and (2) to use as a benchmark dataset to compare with the results of non-standard filtration tests under cyclic loading. During phase-2, another 16 tests were conducted under uniaxial cyclic loading to capture the hydraulic response of subballast filters under simulated dynamic train loading on Australian standard gauge tracks. During static and cyclic tests, the monitored parameters and soil characteristics included time-dependent variations in permeability, internal erosion and axial strain development, pore pressure measurements, and average and local hydraulic gradients contributing to geohydraulic failures such as suffusion, piping and heave. While the parameters compared from static and cyclic loading tests included average and local hydraulic gradients and associated head losses, permeability variations, pre- and post-test relative densities, types of seepage failures, and percentile internal erosion.

Experimental Program

Testing Material and Scheme

The test material consists of 4 non-uniform granular soils including 3 sand-gravel and 1 silt-sand-gravel mixtures (uniformity coefficient C_u = 10, 20, 23, and 304) which are identified as S, MS, MU, and U, respectively (Fig.2). The current soils are symbolised based on their potential of internal erosion determined by the criterion proposed earlier by Indraratna et al. (2015), where S, MS, MU and U represent Stable, Marginally Stable, Marginally Unstable and Unstable soils, respectively. For brevity, this criterion compares the representative particle size of finer fraction of soil at 85th percentile finer by surface area ($d^{f}_{85,AS}$) against the controlling constriction size of its coarser fraction (d^{c}_{c35}), and this would enable one to determine if a given soil would be susceptible to internal erosion under excessive seepage. These soil gradations typically represent the subballast filters to protect erodible subgrades from contaminating the ballast under cyclic loading in railway foundations in New South Wales (NSW) (e.g. Selig and Waters 1994; Haque et al. 2007; Trani and Indraratna 2010; Chung et al. 2012). During the static tests, the normal effective stress (σ'_v) varied from 0 to 100 kPa, while a sinusoidal load ($\sigma'_{min} = 30,\ \sigma'_{max} = 70, \sigma'_{dev} = 40$ and $\sigma'_{mean} = 50$ kPa) was applied to simulate typical heavy haul train movements during the cyclic tests. Cyclic loading frequencies of 5, 10, 20 and 30 Hz were applied to simulate speeds up to 210 km/hr on standard gauge tracks (Christie 2007; Trani and Indraratna 2010; Israr et al. 2016). Notably, cyclic loading was applied from top and hydraulic flow from bottom of test specimens simultaneously, as now shown in Figure 4. Both cyclic and static loads were applied using the same automated hydraulic actuator, which could apply cyclic stresses at frequencies (*f*) up to 40 Hz and normal static stresses up to 850 kPa. For instance, static loading could be simulated using the same actuator by setting cyclic frequency to zero (*f* = 0 Hz).

In this study, each test sample was identified by a three-character acronym, where the first character describes the type of soil such as S, MS, MU, and U, the second character shows the test condition, i.e. S for static and C for cyclic, and the third character represents the magnitude of the static load or cyclic frequency. For instance, specimens U-S100 and U-C30 represent soil U subjected to static normal stress $\sigma'_{vt} = 100$ kPa and cyclic frequency $f = 30$ Hz, respectively.

Sampling and Apparatus

Test specimens were prepared at a relative density of $(R_d) \geq 95\%$ by controlling the mass of dry soil to achieve the minimum void ratio (e_{min}), previously obtained from preliminary compaction tests (ASTM D4253). For instance, the specimens were compacted in 5 discrete layers under a 10 kg surcharge load on a vibrating table (frequency, f = 50 Hz) to achieve the target sample height (after Trani and Indraratna 2010; Israr et al. 2016). To ensure the specimens are compacted uniformly, additional specimens were prepared and examined for; (i) their overall dry density, and (ii) the dry density of small samples cored within each specimen (Indraratna et al. 2015). Similarly, specimen uniformity with respect to particle distribution was ensured by comparing the results of pre- and post-test sieve analyses.

As Fig. 2 shows, the testing apparatus consists of a low-friction polycarbon hydraulic cell (diameter $D_C = 240$ mm and height $H_C = 250$ mm) to accommodate 200 mm long samples. These dimensions of this cell are large enough to yield a ratio R=D_C/d_{100} > 12, where d_{100} = particle size which corresponds to 100% finer by mass. In the past, most hydraulic tests were carried out with apparatuses yielding $4 \leq R \leq 7$ (e.g. Moffat and Fannin 2011; Zou et al. 2013; Indraratna et al. 2015; Israr 2016), because this range would be sufficient to avoid most of the potential boundary effects due to soil erosion.

Two 50 mm diameter pressure cells were placed in the middle and the bottom of the specimens to monitor seepage induced variations in the confining stress. The authors carefully examined the inclusion of pressure cells given that their presence may significantly modify the assumed 1D geometry of the seepage problem and cause local heterogeneities such as non-vertical seepage flow and porosity deteriorations, as these could trigger premature geo-hydraulic failures in the specimens (Moffat and Fannin 2011). For completeness, a total of six independent seepage tests were conducted, i.e. 3 with and 3 without pressure cells, which constitute approximately 2.2% of the total soil volume in a specimen compared to the collective volume of other accessories (e.g. ADR probes, wires, and transducers ≈ 0.4%), as explained elsewhere by Israr et al. (2016). The analysis of results revealed that the porosity variations before the initiation of seepage failures were uniform and independent of the presence of pressure cells. For instance, specimens with and without pressure cells showed similar hydraulic responses, thus for a given soil specimen the failure initiated in the same soil layer and at a unique combination of hydraulic gradient and effective stress. This sufficiently confirmed that the presence of pressure cells had negligible effects on the reported test results of this study.

Saturation and Test Procedure

To avoid any potential disturbances saturation was completed by following the procedure of Israr et al. (2016). For brevity, the specimens were first de-aired by applying up to 120 kPa of back pressure for 2 to 3 hours, and then the de-aired and filtered water was circulated. The test samples were saturated for at least 24 hours under a constant hydraulic head of 50 mm. Notably, complete saturation of a test specimen could be ensured to a satisfactory extent by achieving Skempton's B value > 0.90; and this was completed in 3 to 4 pressure ramps with a very low pressure difference of 10 kPa between the cell and the applied back pressures (after Amini and Hamidi 2014).

An upwards seepage flow was introduced from the bottom of the test chamber at predetermined pressures using an automated hydraulic pump. The variations in hydraulic pressure and associated average and local head losses were monitored with 8 pore water pressure transducers embedded at the inlet, the outlet, and at six different depths inside each sample. The average hydraulic gradient (i_a) is then deduced from the difference between the inflow (p_w^{in}) and outflow pressures (p_w^{out}):

$$i_a = \left(p_w^{in} - p_w^{out}\right)/(h_f \times \gamma_w) \quad (1a)$$

where h_f and γ_w define the thickness of the sample and the unit weight of water, respectively. The local hydraulic gradients (i_{ij}) which evolve as the internal porosity deteriorates is deduced from the differences in head loss, which occurs across discrete layers of soil (Δy):

$$i_{ij} = \left(p_w^j - p_w^i\right)/(\Delta y \times \gamma_w) \quad (1b)$$

where p_w^i and p_w^j are the hydraulic pressures in ith and j^{th} soil layers, respectively. The difference in elevation (potential head) for Eq. 1a is 200 mm, whilst that for Eq. 1b is 25 mm near the boundaries, and 30 mm in the middle of the test specimen.

The test procedure consisted of applying an upward hydraulic flow at pre-requisite pressure levels. The increments of hydraulic gradient (i_a) for the stable sample-S were kept between 3 and 4, for the marginal samples MS and MU between 2 and 3, and for the unstable sample U between 1 and 2. These increments proved adequate to avoid disturbance to the specimens unnecessarily and helped to determine the correct critical hydraulic gradients $i_{cr,exp}$ (Fig. 3). Each test continued for a minimum of 30-40 minutes at a given *i*-value, beyond which steady state flow conditions were generally reached and then the next increment in *i* applied. Not surprisingly, an average test lasted up to 13.5 hours, i.e. some tests ran up to 11 hours (e.g. U-S0 and U-C5) and others up to 16 hours (e.g. U-S100, U-C30, S-C30 and MU-C30). The velocity and turbidity of the effluent were monitored repeatedly during each test by intercepting

the flow over a given period of time. By assuming linear Darcy's law, the saturated hydraulic conductivity was deduced from the slope of the flow curves in Figs. 3a and 3b. The turbidity of the effluent was monitored using Nephelometric Turbidity Unit (NTU) via a portable turbidimeter, while a large, $1m^3$ sedimentation tank was used to capture the eroded fines for post-test forensic analysis. In this study, the hydraulic tests were continued until at least one of the following observations could be made; referred to as geohydraulic failure (Israr and Indraratna 2017; Israr et al. 2016; Indraratna et al. 2015):

(i)- A significant variation in the slope of the flow curves plotted as an applied hydraulic gradient i_a versus effluent flow rate Q_e in litre/min. At the onset of slope variation, the corresponding value of i_a is assumed as the average critical hydraulic gradient $i_{cr,a}$ (Eq. 1),

(ii)- A sudden drop in the magnitude of a local hydraulic gradient i_{ij}, i.e. the local critical hydraulic gradient $i_{cr,ij}$ (Eq. 2),

(iii)- Excessive washout and a marked rise in effluent turbidity ($\gg 60$ NTU), and

(iv)- The development of visible vertical or horizontal channels, which could be identified as heave.

The tested specimens were retrieved in three distinct layers, i.e. top, middle, and bottom, for post-test sieve analysis to determine the extent of internal erosion and any changes in their original particle size distribution (PSD) curves. Notably, internal erosion in the test specimens could be partially represented by the loss of fine particles that may alter their PSD curves; for instance, samples U-S100 and U-C30 experienced 8.9% and 15.7% internal erosion at the particle size d_{10}-level and showed dramatic reductions in the coefficient of uniformity from 304 to 43 and 35, respectively. Nevertheless, changes in the original PSD of the middle layer, or more than 4% of internal erosion, were then considered as rationales to distinguish between internally stable and unstable soils (after Israr et al. 2016; Indraratna et al. 2017; Kenney and

Lau 1985). The geometrical assessments revealed that under static conditions, only soil U was internally unstable (Indraratna et al. 2015), whereas the only existing criterion for cyclic conditions indicated that soils MS, MU, and U were internally unstable (Israr and Indraratna 2017). Nonetheless, the following section evaluates the seepage-induced response experimentally and then re-examines the internal erosion potential of all four soils under both static and cyclic conditions.

Results and Discussion

Table 1 summarises the hydraulic test results of this current study including the test conditions (static or cyclic), the pre- and post-test relative density (R_d), the average critical hydraulic gradient ($i_{cr,a}$), local critical hydraulic gradients ($i_{cr,ij}$), additional hydraulic gradient induced by the pore water pressure ($i_{\Delta u}$), and the percentage of internal erosion and type of seepage induced failure (i.e. heave, heave-piping or suffusion). The following sections elaborate on the specific details of the hydraulic test results.

Hydraulic Response under Static and Cyclic Loading

Figure 3 shows the results of hydraulic tests on fully compacted soil U ($R_d \geq 95\%$), subjected to static loading magnitudes of 0, 25, 50 and 100 kPa (Table 1). As Fig. 3a shows, the flow curves plotted as average hydraulic gradient i_a versus effluent flow rate Q_e developed steadily with the increasing magnitude of static loading. The saturated permeability of the soil samples was deduced from the slope of the initial portion of the flow curves by assuming linear Darcy's law. A comparison of the pre- and post-test results reveals that the saturated permeability of soils remains independent of the magnitude of static loading (Table 1). Notably, the flow rate does not vary significantly for very small lengths of flow curves within the laminar regime e.g. e.g. up to $i_a \leq 0.1$ and $Q_e \leq 0.04$ lit/min for the specimen U, as now shown in Fig. 3a (inset), where the slopes of flow curves remained relatively unchanged. However, we know that the

slopes would decrease markedly due to higher hydraulic head losses at particle contact levels under larger effective stress magnitudes until the occurrence of suffusion (Langroudi et al. 2013; Zou et al. 2013; Qing-fu et al. 2014). So this flow rate is not just a function of sample dimensions and specimen permeability, but also influenced by the external hydraulic loads. Notably, this is consistent with the previous studies which report that the suffusion potential decreases with the increase in static loading magnitude (e.g. Li and Fannin 2008; Moffat and Fannin 2011; Moffat and Herrera 2014; Israr et al. 2016).

The inception or onset of suffusion in soil U is characterised by a steep increase in the rate of effluent flow with turbidity in excess of 60 NTU, and a marked variation in the shape of the flow curve (Fig. 3a). Notably, the magnitude of average critical hydraulic gradient $i_{cr,a}$ for suffusion increased proportionally from 0.26 to 25.5 with the magnitude of static load increasing from 0 to 100 kPa. Figure 3b shows the time histories of axial strain for soil U, with no significant compression prior to suffusion, although limited internal erosion continues at all i_a-values. The shapes of the strain curves remain identical before suffusion (i.e. excessive erosion of fines), which increases the void ratio and allows particles to rearrange and compress further, as shown by the sudden increase in the axial strain values (Fig. 3b). Nevertheless, the time for suffusion to commence in soil U increased when the static loading increased from 0 to 100 kPa; this shows the stabilising effects of static loading.

Figure 4 shows the flow curves and axial strain histories for compacted soil U ($R_d \geq 95\%$), subjected to cyclic loading at frequencies of 5, 10, 20, and 30 Hz. Unlike under static loading, the magnitudes of $i_{cr,a}$ for soil U decreases from 29.4 to 24.7 when the cyclic frequency increases from 5 to 30 Hz. The cyclic loading conditions reduce the pre-test permeability of soil U in proportion to the cyclic loading frequency (Table 1). Not surprisingly, the axial strain histories under cyclic loading show significant initial compression before reaching an almost

constant strain condition termed as elastic shakedown, until suffusion commences. During the elastic shakedown, the specimen response remains generally rigid with almost no variations in the strain rates that can be attributed to particle rearrangements and some limited erosion. Nevertheless, the time for elastic shakedown to occur appears to be frequency dependent, e.g. 360 min for sample U-C5 (i.e. at 5 Hz) compared to 110 min for sample U-C30 (at 30 Hz).

As Figures 5a and 5b show, the time for elastic shakedown to commence in samples S and MS decreases markedly when the loading frequency increases from 5 to 30 Hz. Notably, up to 95% strain energy has accumulated at the elastic shakedown and this has had a significant influence on the development of excess pore water pressure (Polito et al. 2008; Seed et al. 1983), and then the inception of geohydraulic failure (Israr et al. 2016). Nevertheless, the strain rate beyond elastic shakedown remains negligible until and after the onset of heave in samples S, where variations in strain evolve due to particle rearrangements. However, no significant axial strain develops, even after the inception of heave, due to negligible erosion of finer fractions from the internally stable samples S. However, there appears to be a marked increase in axial strain after the inception of suffusion due to the significant erosion of finer fractions from an internally unstable sample U.

An analysis of the time histories of local hydraulic gradients (i_{ij}) for sample U subjected to static and cyclic loading is shown in Figs. 6a and 6b, respectively. During a static test U-S50 (under a static normal stress of 50 kPa), suffusion initiated in soil layer-56, i.e. at 55 mm to 85 mm from the top at a local hydraulic gradient is $i_{cr,ij} = 21.9$, whereas during a cyclic test U-C5 (at 5 Hz and mean normal stress of 50 kPa), suffusion occurred in the same soil layer-56 but at a greater value of $i_{cr,ij} = 34.5$. This discrepancy in critical hydraulic gradients could be explained by the development of excess pore water pressure due to cyclic loading that induced

a greater i_{ij} at the particle level which, in corroboration with the externally applied hydraulic gradients i_a, triggered suffusion.

Figures 7a and 7b show the effects of cyclic frequency and normal effective stress on the magnitudes of critical hydraulic gradients, respectively. Fig. 7a shows that as the $i_{cr,a}$-values decrease, the $i_{cr,ij}$-values generally increase with the increase in loading frequency, which indicates that the pore water pressure that develops under cyclic loading becomes excessive at a higher loading frequency. The decreasing $i_{cr,a}$-values and increasing $i_{cr,ij}$-values indicate that less external hydraulic pressure is required, while greater internal hydraulic pressure is developed at higher cyclic loading frequencies, thus causing premature geohydraulic failures such suffusion, piping and heave (Israr et al. 2016). Not surprisingly, the values of $i_{cr,a}$ and $i_{cr,ij}$ increase with the increase in static loading from 0 to 100 kPa, thus showing the stabilising effects of static loading. For instance, soil under a static load of 25 kPa would require much less $i_{cr,a}$ and $i_{cr,ij}$ for geohydraulic failures to commence, compared to that under 100 kPa, thus showing greater internal stability at 100 kPa (see Table 1).

Effects of Pore Pressure Generation under Cyclic Loading

In this study, the magnitude of pore water pressure generated during hydraulic tests under cyclic loading was deduced using the method of Israr et al. (2016). For brevity, the external head loss across the whole sample (h_w^t) could be given by (Eq. 2):

$$h_w^t = \frac{p_w^{in} - p_w^{out}}{\gamma_w} \quad (2)$$

where h_w^{in} and h_w^{out} represent the external inflow and outflow hydraulic heads applied to the soil specimens. Similarly, the sum of local head losses (H_w^t) was computed using the following expression (Eq. 3):

$$H_w^t = \sum_{i=n}^{j=n+1} \frac{p_w^j - p_w^i}{\gamma_w} \quad (3)$$

where h_w^i and h_w^{i+1} represent the local inflow and outflow seepage heads for a discrete soil layer inside a specimen.

Now, the equivalent hydraulic head due to induced pore water pressure can be computed as the difference between the overall internal head loss H_w^t and external head loss h_w^t, as follows:

$$\Delta u = (H_w^t - h_w^t) \times \gamma_w \quad (4)$$

Not surprisingly, this difference is negligible for the static tests, unlike in the case of cyclic tests where significant differences are recorded (Table 1). The additional pore pressure gradient ($i_{\Delta u}$) due to the generation of pore water pressure under cyclic loading was given the following dimensionless expression:

$$i_{\Delta u} = \Delta u / \gamma_w \times \Delta y \quad (5)$$

where Δy is the depth of the soil layer, as shown in Fig. 8. Table 1 summarises the $i_{\Delta u}$-values for current test specimens, where MU and U exhibit manifolds higher $i_{\Delta u}$-values compared to S and MS. For instance, under cyclic frequency of 5 Hz, samples S, MS, MU, and U exhibited $i_{\Delta u} = 5.9, 3.1, 10.5$ and 12.5, respectively. Moreover, the magnitude of $i_{\Delta u}$ increased steadily with that of cyclic frequency, e.g. at 30 Hz frequency, S, MS, MU and U exhibited $i_{\Delta u} = 7.7, 4.3, 14.9$ and 15.7, respectively.

In practice, the accumulated excess pore water pressure is often quantified in terms of normalized pore pressure ratio $n_{\Delta u}$, which is defined as the ratio of the residual excess pore pressure Δu to the initial effective confining stress σ'_{co} (Polito et al. 2008). The value of $n_{\Delta u}$ varies between zero (i.e., no excess pore pressures) and one (i.e., zero effective stress or fluidization), thus providing more insight than the magnitude of Δu alone.

$$n_{\Delta u} = \frac{\Delta u}{\sigma'_{co}} \quad (6)$$

where $n_{\Delta u}$ is the normalised pore pressure ratio, $\sigma'_{co} (= \sigma'_{mv} \times (1 + 2K_0)/3)$ is the mean effective confining stress, K_0 $(= 1 - sin\,\emptyset')$ is the coefficient of earth pressure at rest, and $\emptyset'$ is the drained angle of internal friction. In this study, the mean effective confining stress (σ'_{co}), could be measured directly by the embedded load cells. Now, by using the relationship for σ'_{co} in Eq. 6 and then rearranging to obtain an expression for the pore pressure ratio gives:

$$n_{\Delta u} = \frac{3 \times (H_w^t - h_w^t) \times \gamma_w}{\sigma'_{mv} \times (1+2K_0)} \quad (7)$$

Eq. 5 and 7 indicate that $i_{\Delta u}$ is dependent on the effective confining stress, which is likely to vary significantly with the magnitude of applied cyclic loading that in this study is kept similar for all tests, i.e. $\sigma'_{min} = 30$ kPa and $\sigma'_{max} = 70$ kPa. Figure 9 shows the time histories of Δu during the cyclic tests where the magnitude of Δu accumulates over time and reaches its maximum value at the critical onset of geohydraulic failure, i.e. heave in soil specimen S and suffusion in rest of the specimens. Notably, specimens S and MS had relatively smaller and similar values of Δu at all frequencies, unlike MU and U, which had greater magnitudes of Δu and larger variations at higher frequencies. This shows that S and MS can be considered as more suitable protective filters in severe cyclic conditions rather than MU and U. Nevertheless, the decreasing trends of Δu after the inception of failure indicate a release of strain energy, which is consistent with the previously discussed sudden variations in axial strain histories. Figure 10 shows the variations in the magnitudes of Δu, $n_{\Delta u}$, and $i_{\Delta u}$ induced due to the simulated cyclic loading frequencies and associated train speeds for a standard gauge track. Additional results from Israr et al. (2016) are also plotted in Fig. 10, and all these results are summarised in Table 1.

Proposed Model

The cyclic loads impart a significant magnitude of strain energy to the soil specimens during loading and unloading cycles, as shown by the axial strain histories discussed in the previous sections (see Figs. 4 and 5). While some portion of this energy dissipates safely due to drag and the frictional characteristics of soils (Polito et al. 2008), the remaining energy continues to accumulate and this may cause significant pore water pressure to develop (Indraratna et al. 2017; Alobaidi and Hoare 1998). In this study, the comparisons between the external and internal hydraulic head losses in a soil specimen can determine the pore pressure generated due to dynamic loading. The following section presents a proposed semi-empirical model to quantify the development of pore water pressure using the framework of strain energy dissipation in granular soils.

A normalised pore pressure ratio ($n_{\Delta u}$) is introduced to capture the pore water pressure generated due to cyclic loading; this in turn is a function of the initial effective confining stress σ'_{co} and the dissipated strain energy per unit volume of soil ΔW (Berrill and Davis 1985):

$$n_{\Delta u} = A\left(\frac{\Delta W}{\sigma'_{co}}\right)^{B} \quad (8)$$

The magnitude of ΔW can be given by the area under the stress-strain hysteresis curve (Green et al. 2000):

$$\Delta W = 0.5 \times \sum_{i=1}^{n}\left(\sigma'_{d,i+1} + \sigma'_{d,i}\right)\left(\varepsilon_{a,i+1} - \varepsilon_{a,i}\right) \quad (9)$$

where, ΔW = dissipated energy per unit volume of soil

$\sigma'_{d,i}, \sigma'_{d,i+1}$ = ith and i+1th increments in cyclic deviator stress σ'_{min}

$\varepsilon_{a,i}, \varepsilon_{a,i+1}$ = ith and i+1th increments in axial strain

n = total number of load increments

A and B = Empirical coefficients determined from hydraulic tests under cyclic loading. Given the magnitude of cyclic deviator stress was constant, Eq. 9 becomes:

$$\Delta W = \Delta\sigma_d' \sum_{i=1}^{n} \left(\varepsilon_{a,i+1} - \varepsilon_{a,i}\right) \quad (10)$$

$$\Delta W = \Delta\sigma_d' \times \varepsilon_a \quad (11)$$

The net axial strain (ε_a) evolves with time by dynamic compaction due to cyclic loading, and as a function of the number of loading cycles and frequency. During 1-dimensional compression, the axial strain evolves rapidly until the elastic shakedown level (permanent plastic deformation) is reached, and then becomes constant (purely elastic). Using an exponential function for axial strain in Eq. 11 yields (Trani and Indraratna 2010):

$$\Delta W = \Delta\sigma_d' \times \varepsilon_f \left(1 - e^{-tf/k_n}\right) \quad (12)$$

where, $t =$ Time for the application of cyclic loading (sec)

$f =$ Cyclic loading frequency (Hz)

$k_n =$ Scaling factor equal to $N_{max}/10$

$N_{max} =$ Maximum number of load cycles applied to the soil.

Substituting Eq. 12 into Eq. 8 gives:

$$n_{\Delta u} = A \left(\frac{\Delta\sigma_d' \times \varepsilon_f \left(1 - e^{-tf/k_n}\right)}{\sigma_{min}'}\right)^B \quad (13)$$

Model Parameters

In Eq. 13 above, the empirical factor *A* is the cyclic loading coefficient, which accounts for the magnitude of applied mean cyclic stress σ_{mv}' and is given by (Israr 2016):

$$A = \sigma_{mean}'/10 = \left(\frac{\sigma_{min}' + \sigma_{max}'}{2}\right)/10 \quad (14)$$

where σ_{min}' and σ_{max}' represent the magnitudes of minimum and maximum cyclic loads (i.e. unloading and loading), respectively.

The empirical factor *B* is the hydraulic conductivity coefficient, which captures the reduction in permeability due to dynamic compaction under cyclic loading. Figure 11 shows the correlation between *B* and the permeability reduction ratio k_i/k_f which results from the cyclic densification of the current test results. The following empirical linear relationship is observed with a high coefficient of correlation (i.e. $R^2 > 0.95$):

$$B = 0.065\left(\frac{k_i}{k_f}\right) + 0.60 \quad (15)$$

where k_i and k_f define the initial permeability and the final permeability due to cyclic densification (i.e. before the inception of geohydraulic failure), respectively.

Discussion and Model Validation

Figure 12 shows the cyclic response of current samples that can be divided into three distinct phases, as follows:

(I) Pre-shakedown: cyclic densification occurs in the form of permanent deformation (i.e. axial strain) and the soil response remains purely plastic,

(II) Post-shakedown: cyclic loading does not incur permanent deformations and the soil response remains elastic. Nonetheless, the physical impact of vibrations may result into rearrangement of particles and yield negligible axial strain compared to phase-I, as observed in some of the current test results.

(III) Post-critical: geohydraulic failures occur such as heave in internally stable and suffusion in unstable soils. Permanent deformation occurs such as marked axial strain due to cyclic densification and internal erosion in tandem and the soil response is purely plastic, just like phase-I.

In essence, during phases I and III, the specimen response remains generally identical and may probably be followed by a rigid response (e.g. phase II). This cycle of accumulation and

dissipation (A-D) from phase I to III continues, and the net result is in the form of excessive settlement due to accumulated axial strains. Figure 13 shows the mechanism of axial strain developing due to the cycles of accumulation and dissipation due to the application of cyclic loading. Nevertheless, the resulting axial strain may exceed tolerable serviceability limits for many high-speed track substructures.

Not surprisingly, the current specimens initially show permanent (plastic) deformation due to cyclic loading in phase I until they reach elastic shakedown, which occurs in the initial phase of cyclic loading. For instance, sample MU under 20 Hz cyclic loading (MU-C20) reaches the elastic shakedown level in 180 minutes (i.e. number of load cycles, N < 220,000), but after this the specimen response remains purely rigid, and there is no variation in axial strain until the inception of geohydraulic failure, that occurs at time t = 500 minutes (i.e. N = 600,000). As a result of failure (i.e. heave or suffusion), the specimens show marked permanent deformation in the form of significant axial strain, as shown by the increasing trends of strain histories discussed in the previous sections. For instance, up to 2.33% of axial strain is recorded in the only cycle of accumulation and dissipation simulated in this study for sample-U (Table 1). In essence, before the soils become unstable, more than 95% strain energy accumulates in the initial elastic shakedown regime, and the specimens show permanent deformation.

The proposed model was validated with the experimental results of this current study (Table 1) and those adopted from the published literature presented (Table 2). The model parameters adopted from both studies are presented separately in Table 3, including the loading frequency *f*, the permeability ratio k_i/k_f, the cyclic loading coefficient *A* and the hydraulic conductivity factor *B*. For the data reported in Table 3, Fig. 14 plots the observed $n_{\Delta u}$-values against those predicted from Eq. 13. As shown, there is a close agreement between the two $n_{\Delta u}$-values, where

most data points closely follow the line of equality with less than 6% standard error of mean; this may be acceptable as a preliminary analysis for most practical purposes.

Limitations of this Study

This study is focused on the analysis of granular soils subjected to simultaneous one-dimensional upward flow and downward mechanical loading, which in practice would simulate real life subballast filter and drainage layers in railway substructures. Note that the hydro-mechanical equilibrium and the inclined seepage paths in full-scale problems may be quite different from those considered here for simplified laboratory modelling, which is often one-dimensional. In this study, a fixed magnitude of sinusoidal load, i.e. $\sigma'_{min} = 30,\ \sigma'_{max} = 70, \sigma'_{dev} = 40$ and $\sigma'_{mean} = 50$ kPa with a cyclic stress ratio of 0.67 and frequency up to 30 Hz was applied to simulate a heavy-haul train operating at speeds up to 210 km/hr on a standard gauge track. Nonetheless, as a common limitation for most laboratory studies, the scale of the testing may not be comparable to the actual dimensions of most practical problems.

Conclusions

This study attempted to model the generation of pore water pressure in subballast filters subjected to cyclic loading at varying frequencies in the laboratory, and presented a framework to investigate the generation of pore pressure in soft saturated subgrades. Based on the principal findings of the current results, the proposed model and its validation, the following conclusions can be drawn:

- The application of static loading stabilised the specimens by increasing the magnitude of critical hydraulic gradients (i_{cr}), whereas cyclic loading tended to destabilise them by decreasing the magnitudes of i_{cr} for geohydraulic failures. For instance, only specimen U could be characterised as internally unstable under static conditions, while under cyclic loading, only specimen S showed internal stability.

- In addition to constant physical perturbation, cyclic loading induced significant build-up of excess pore pressure as a function of loading frequency. The other factors, which markedly influenced the generation of pore pressure, included reduced permeability attributed to cyclic densification, the number of loading cycles, and the axial compression of specimens.
- The pore pressure induced at higher frequencies (10 to 30 Hz) triggered excessive internal erosion in the current specimens, which caused premature suffusion in internally unstable and marginal soils (MS and MU). Nonetheless, despite showing internal stability during the static tests, both MS and MU suffered from severe internal erosion under cyclic conditions and therefore deemed internally unstable.
- In this study, the compression of specimens under cyclic loading could be divided into three distinct phases before and after the elastic shakedown level; namely (I) pre-shakedown plastic, (II) post-shakedown elastic, and (III) post-critical plastic phases. All the reductions in porosity and permeability due to cyclic densification occur in the plastic phases I and III, where strain energy accumulates. Maximum pore pressure generates in the elastic phase II where the specimens possess minimum hydraulic conductivities.
- The cyclic strain energy is released to induce pore water pressure as a function of the permeability reduction and effective confining stress. In this regard, an energy based pore pressure model has been proposed and successfully validated through current and published test results.
- Notably, four out of seven soils examined in this study exhibited internal instability during cyclic filtration tests (i.e. MS, MU, U and G). This implies that the current industry practices for selecting subballast filters may include significant potential for internal instability under cyclic loading.

The current model can reasonably estimate the excess pore pressure and facilitate hydro-mechanical assessment of internal stability to ensure the longevity of subballast filters under

cyclic loading conditions. However, its applications to naturally erodible subgrade soils under different conditions warrant further investigations. While the current propositions may be recommended as a reliable tool for preliminary analysis only prior to detailed investigations, caution must still be exercised when applying the proposed model to soils with markedly different properties in field problems.

Acknowledgement

The financial support provided in the form of Faculty Development Program and International Postgraduate Tuition Award scholarships by University of Engineering and Technology Lahore (Pakistan) and University of Wollongong (Australia), respectively. The technical support from laboratory staff of Centre for Geomechanics and Railway Engineering (GRE), University of Wollongong, is gratefully acknowledged.

Notation

Following symbols are used in this paper:

CSD and PSD = Particle and constriction size distributions, respectively;

C_u = Coefficient of uniformity;

D_C = hydraulic cell diameter (mm);

$d_{85,AS}^{f}$ = 85th percentile finer by surface area (mm);

d_{c35}^{c}= controlling constriction size of coarser fraction (mm);

d_x = Particle size corresponding to x percentile finer by mass (mm);

e_{min} = Minimum index void ratio;

f = Cyclic loading frequency (1/sec);

H_C = Hydraulic cell height (mm);

h_f = Thickness of soil sample (mm);

h_w^{in} and h_w^{out} = Inflow and outflow hydraulic head losses, respectively (m);

h_w^t and H_w^t = Sum of external and internal head losses, respectively (m);

$i,\ i_a$ and i_{ij} = Expressions for applied, average and local hydraulic gradients, respectively;

$i_{cr,exp}$ and $i_{\Delta u}$ = Observed critical and pore pressure hydraulic gradients, respectively;

$i_{cr,ij}$ and $i_{cr,a}$ = Local and average critical hydraulic gradients, respectively;

K_0 = Coefficient of earth pressure at rest;

k_i and k_f = Initial and final hydraulic conductivity (m/sec);

k_n = Scaling factor;

N and N_{max} = Number of cycles and maximum number of cycles applied, respectively;

$n =$ Total number of load increments;

Q_e = Volumetric flow rate of effluent (m3/sec);

R_d = Relative density of soil;

p_w^i and p_w^j = Hydraulic pressures at ^{i}th and ^{j}th points, respectively (kPa);

p_w^{in} and p_w^{out} = Inflow and outflow hydraulic pressure, respectively (kPa);

R = Ratio of cell diameter and largest particle size;

$n_{\Delta u}$ = Normalized pore water pressure ratio;

t = Time of application of cyclic loading (sec);

γ_w and γ_s = Unit weights of water and soil, respectively (kN/m^3);

$\varepsilon_{a,i+1}$and $\varepsilon_{a,i}$ = The ith and i+1th increments in axial strain, respectively;

ε_f = Frictional component of axial strain;

$\sigma'_{d,i}$ and $\sigma'_{d,i+1}$ = The ith and i+1th increments in cyclic deviator stress, respectively (kPa);

σ'_v, σ'_{min}, σ'_{max}, σ'_{dev} and σ'_{mean} = Expressions for vertical, minimum, maximum, deviator and mean effective stresses, respectively (kPa);

σ'_{co} and σ'_{mv} = Effective confining and mean vertical effective stresses, respectively (kPa);

$\emptyset'$ = Drained angle of internal friction (degrees);

$\Delta\sigma'_d$ = Mean deviator stress (kPa);

ΔW = Strain energy per unit volume;

Δu = Excess pore water pressure (kPa); and

Δy = thickness or depth of soil layer (mm).

References

Alobaidi, I. M., and Hoare, D. J. (1998). “Qualitative criteria for anti-pumping geocomposites.” *Geotextiles and Geomembranes.,* 16, 221-245.

American Society for Testing and Materials (ASTM). (2006) “Standard test methods for maximum index density and unit weight of soils using a vibratory table,” *ASTM* D4253-06, West Conshohocken, Pa.

Berrill, J. B., and Davis, R. O. (1985). “Energy dissipation and seismic liquefaction of sands: revised model.” *Soils Found.,* 25(2), 106–118.

Burenkova, V. V. (1993). “Assessment of suffusion in non-cohesive and graded soils.” Filters in geotechnical and hydraulic engineering, J. Brauns, M. Heibaum, and U. Schuler, eds., Bakema, Rotterdam, The Netherlands, 357-360.

Chang, D. and L. Zhang (2013). “Critical Hydraulic Gradients of Internal Erosion under Complex Stress States.” *J. Geotech. Geoenviron. Eng.*,139(9), 1454-1467.

Christie, D. (2007). “Bulli field trial: Vertical and lateral pressure measurement.” *Rail CRC Seminar,* seminar conducted at the University of Wollongong.

Chung Ip, M., Haque, A. and Bouazza, A. (2012). “Influence of cyclic stress pulse shapes on filtration behavior of railway subballast.” *J. Geotech. Geoenviron. Eng.,* 138(2), 230-235.

Fourie, A. B., Copeland, A. M., and Barrett, A. J. (1994). "Optimization of the as-placed properties of hydraulic backfill." *J. South African Instt. Min. and Met.*, 94(8), 199-210.

Green, R. A., Mitchell, J. K., and Polito, C. P. (2000). “An energy-based pore pressure generation model for cohesionless soils.” *Proc., John Booker Memorial Symposium-Developments in Theoretical Geomechanics*, D. W. Smith and J. P. Carter, eds., Balkema, Rotterdam, The Netherlands, 383–390.

Gutenberg, B., and Richter, C. F. (1942). Earthquake magnitude. Intensity, energy and acceleration. *Bull. Seimol. Soc. Amer.,* (32), 163-191.

Haque, A., Kabir, E. and Bouazza, A. (2007). “Cyclic filtration apparatus for testing subballast under rail track.” *J. Geotech. Geoenviron. Eng,* 133(3), 338-341.

Indraratna, B., Israr, J., and Li, M. (2017). “Inception of geohydraulic failures in granular soils- an experimental and theoretical treatment.” *Geotechnique,* http://dx.doi.org/10.1680/jgeot.16.P.227 (In Press).

Indraratna, B., Israr, J., and Rujikiatkamjorn, C. (2015). “Geometrical method for evaluating the internal instability of granular filters based on constriction size distribution.” *J. Geotech. Geoenviron. Eng.,* (DOI: 10.1061/(ASCE)GT.1943-5606.0001343), 1-14.

Indraratna, B., Nguyen, V. T., and Rujikiatkamjorn, C. (2012). "Hydraulic conductivity of saturated granular soils determined using a constriction-based technique." *Can. Geotech. J.* 49(5), 607-613.

Israr, J. (2016). Internal instability of granular filters under cyclic loading. *PhD thesis,* University of Wollongong, Wollongong, Australia.

Israr, J., and Indraratna, B. (2017). Internal stability of granular filters under static and cyclic loading. *J. Geotech. Geoenviron. Eng.*, 04017012 (DOI: 10.1061/(ASCE)GT.1943-5606.0001661).

Israr, J., Indraratna, B., and Rujikiatkamjorn, C. (2016). “Laboratory modelling of the seepage induced response of granular soils under static and cyclic conditions” *Geotech. Testing. J.*, 39(5), 1-18 (DOI: 10.1520/GTJ20150288)

Kenney, T. C., and Lau, D. (1985). “Internal stability of granular filters.” *Can. Geotech. J.,* 22, 215–225.

Koerner, G. R., Koerner, R. M., and Martin, J. P. (1994). “Design of landfill leachate- collection filters.” *J. Geotech. Geoenviron. Eng.,* 120, No. 10, 1792-1803.

Moffat, R. and Fannin, R. J. (2011). “A hydromechanical relation governing the internal stability of cohesionless soil.” *Can. Geotech. J.* 48, No. 3, 413–424.

Nemat-Nasser, S., and Shokooh, A. (1979). “A Unified Approach to Densification and Liquefaction of Cohesionless Sand in Cyclic Shearing.” *Canadian Geotechnical Journal* 16: 659-678.

Polito, C. P., Green, R. A., and Lee, J. (2008). “Pore pressure generation models for sands and silty soils subjected to cyclic loading.” *J. Geotech. Geoenviron. Eng.*, 134(10), 1490-1500.

Sansalone, J., Kuang, X., and Rainieri, V. (2008). “Permeable pavement as a hydraulic and filtration interface for urban drainage.” *J. Irrig. Drain. Eng.* 134(5), 666-674.

Sassa, S., and Sekiguchi, H. (1999). “Wave-induced liquefaction of beds of sand in a centrifuge.” *Geotechnique* 49(5), 621-638.

Seed, H. B., Idriss, I. M., and Arango, I. (1983). “Evaluation of liquefaction potential using field performance data.” *J. Geotech. Engrg.*, 109(3), 458–482.

Seed, H.B., and Idriss, I.M. (1971). “Simplified Procedure For Evaluation Soil Liquefaction Potential” *Journal of the Soil Mechanics and Foundations Division*, 97(9), 1249-1273.

Selig, E. T., and Waters, J. M. (1994). *Track geotechnology and substructure management*. London: Thomas Telford.

Trani, L. D. O. and Indraratna, B. (2010). “Assessment of Subballast Filtration under Cyclic Loading.” *J. Geotech. Geoenviron. Eng*, 136(11), 1519-1528.

Xiao, M. and Shwiyhat, N. (2012). "Experimental investigation of the effects of suffusion on physical and geomechanic characteristics of sandy soils." *J. Geotech. Testing.* 35(6), 890-900.

Xiao, M., Reddi, L.N., and Steinberg, S. (2006). “Effect of vibrations on pore fluid distribution in porous media.” *Transport in Porous Media,* 62(2), 187-204.

Youd, T. L., Idriss, I. M., Andrus, R. D., and Arango, I. (2001). “Liquefaction resistance of soils: Summary report from the 1996 NCEER and 1998 NCEER/NSF workshops on evaluation of liquefaction resistance of soils.” *J. Geotech. Geoenviron. Eng.*, 127(10), 817–833.

Zou, Y., Chen, Q., Chen, X., and Cui, P. (2013) “Discrete numerical modelling of particle transport in granular filters.” *Comput. Geotech.*, 32(5), 340–57.

List of Figures

List of Tables

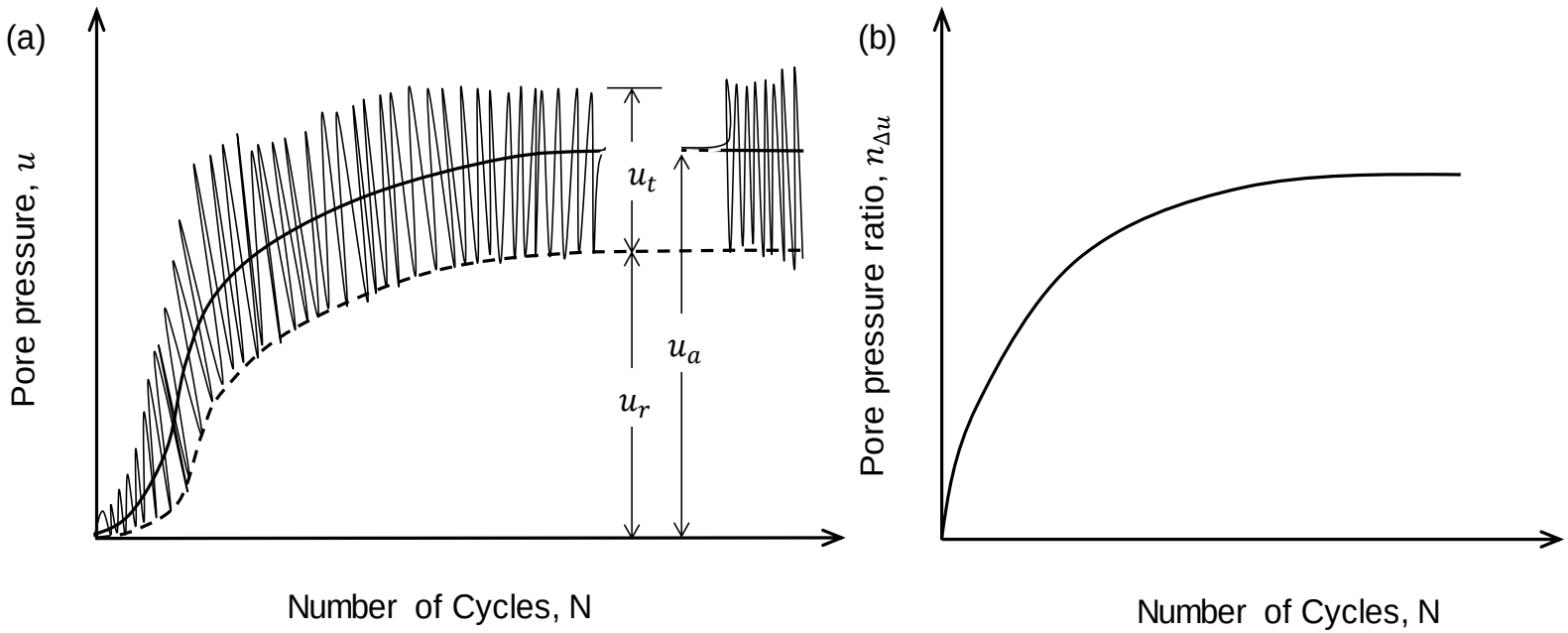
(a)
Pore pressure, u
u_t
u_a
u_r
Number of Cycles, N
(b)
Pore pressure ratio, $n_{\Delta u}$
Number of Cycles, N

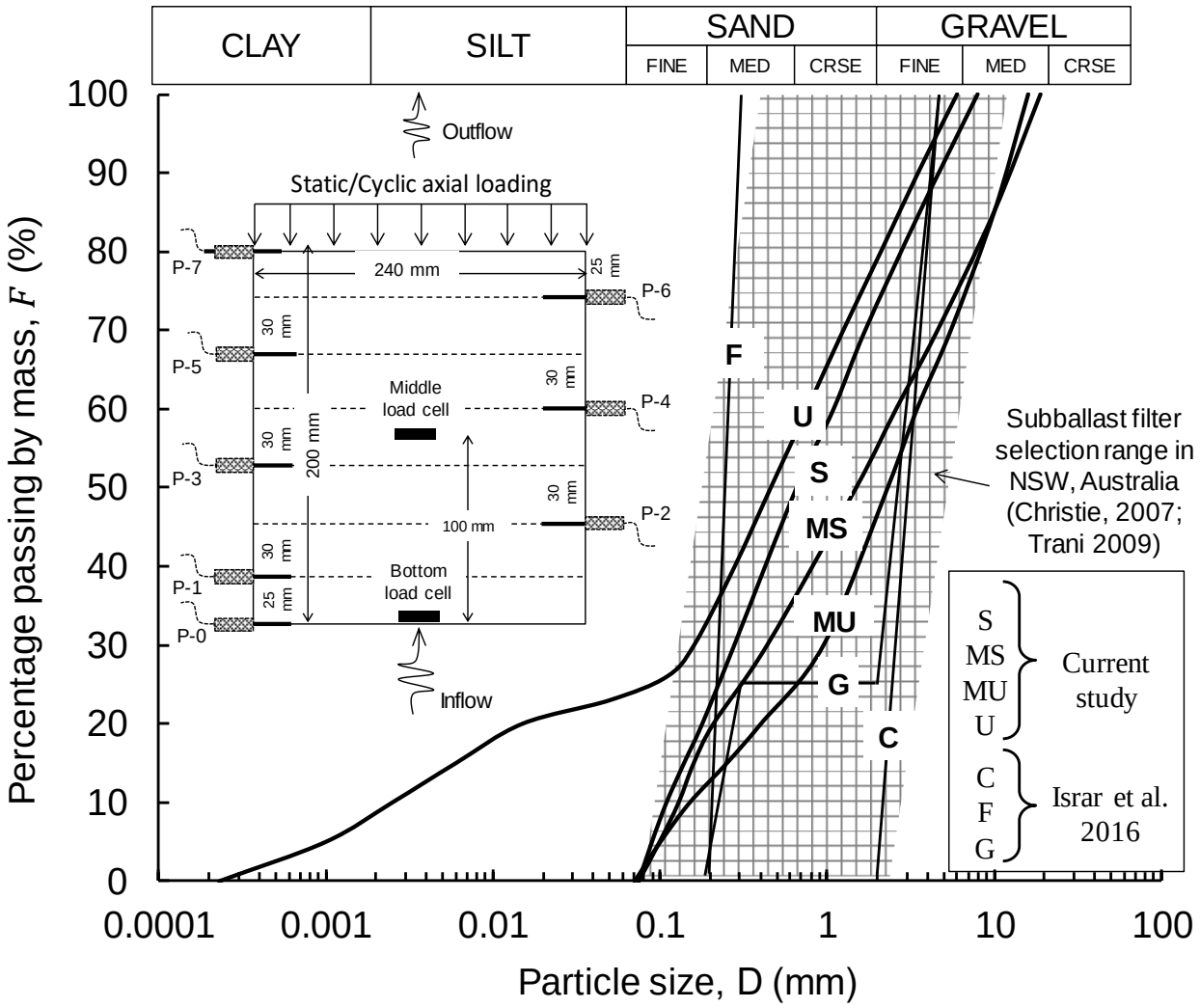
CLAY
SILT
SAND
GRAVEL
FINE
MED
CRSE
FINE
MED
CRSE
Outflow
Static/Cyclic axial loading
240 mm
25 mm
30 mm
30 mm
30 mm
30 mm
30 mm
25 mm
200 mm
100 mm
Middle load cell
Bottom load cell
P-7
P-6
P-5
P-4
P-3
P-2
P-1
P-0
Inflow
F
U
S
MS
MU
G
C
Subballast filter selection range in NSW, Australia (Christie, 2007; Trani 2009)
S
MS
MU
U
Current study
C
F
G
Israr et al. 2016
Percentage passing by mass, F (%)
Particle size, D (mm)
0
10
20
30
40
50
60
70
80
90
100
0.0001
0.001
0.01
0.1
1
10
100

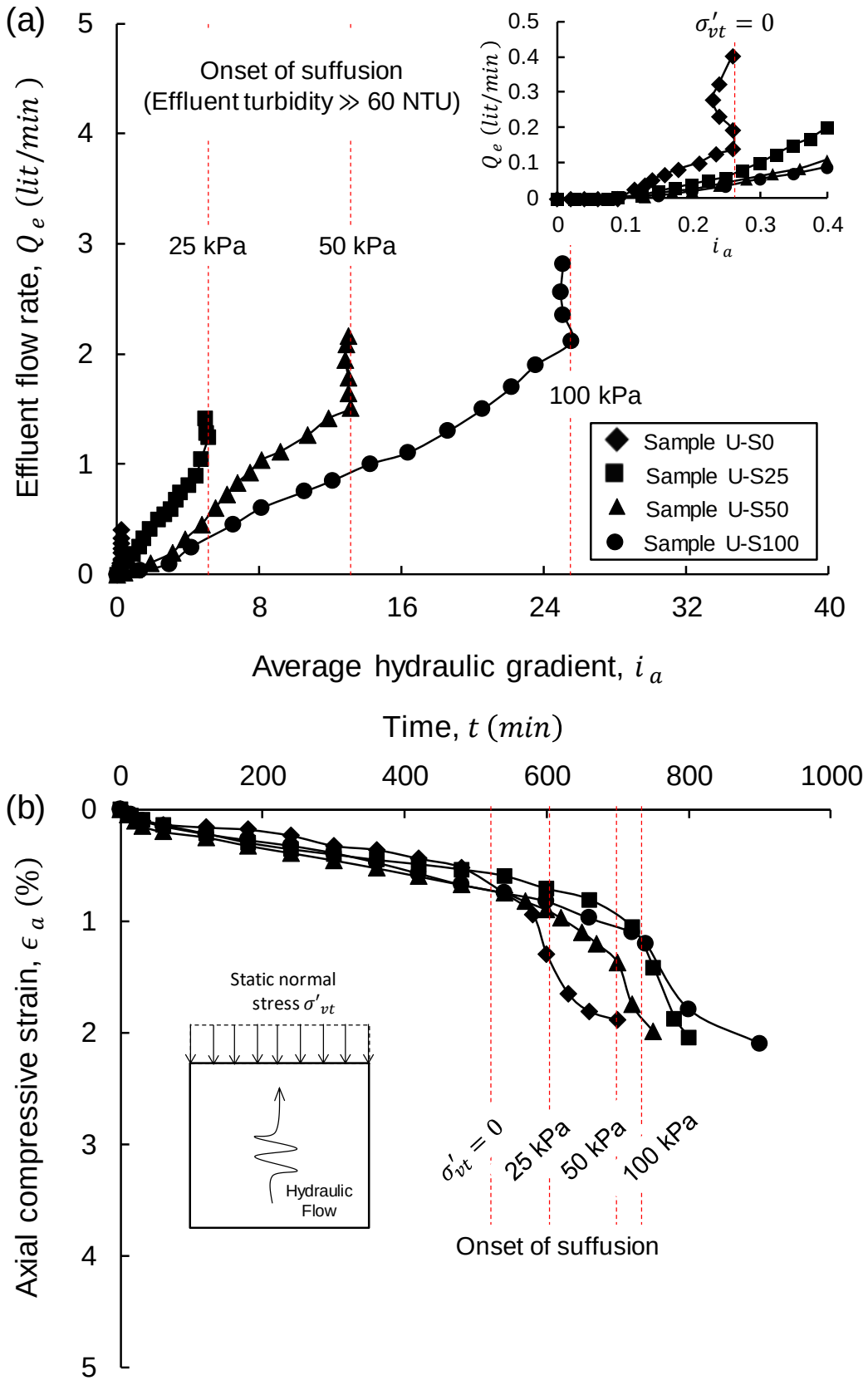
(a)
Effluent flow rate, Q_e (lit/min)
Onset of suffusion
(Effluent turbidity ≫ 60 NTU)
25 kPa
50 kPa
100 kPa
$\sigma'_{vt} = 0$
Q_e (lit/min)
i_a
Sample U-S0
Sample U-S25
Sample U-S50
Sample U-S100
Average hydraulic gradient, i_a
Time, t (min)
(b)
Axial compressive strain, ϵ_a (%)
Static normal stress σ'_{vt}
Hydraulic Flow
$\sigma'_{vt} = 0$
25 kPa
50 kPa
100 kPa
Onset of suffusion

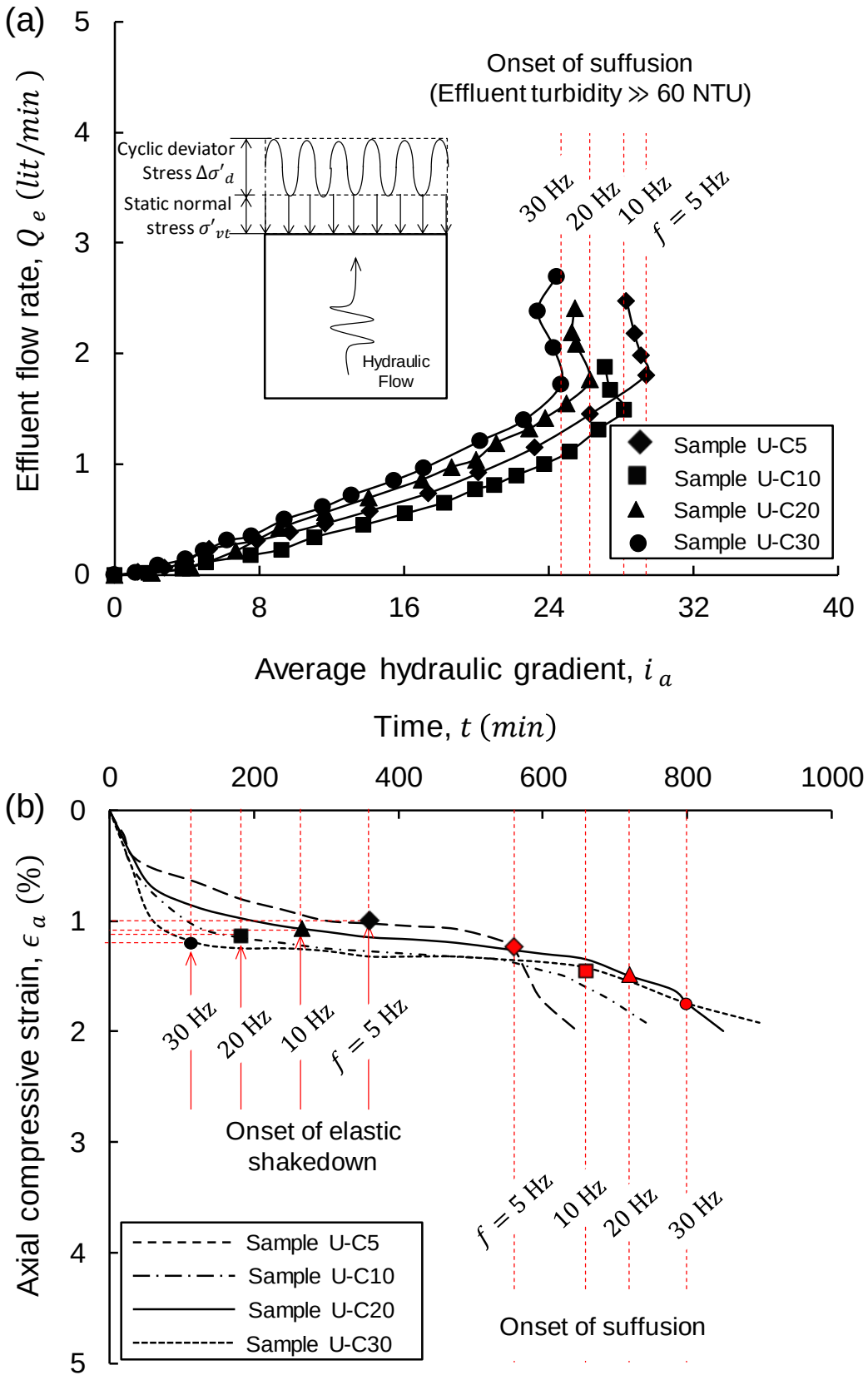
(a)
Effluent flow rate, Q_e (lit/min)
Onset of suffusion
(Effluent turbidity ≫ 60 NTU)
Cyclic deviator Stress $\Delta\sigma'_d$
Static normal stress σ'_{vt}
Hydraulic Flow
30 Hz
20 Hz
10 Hz
$f = 5$ Hz
Sample U-C5
Sample U-C10
Sample U-C20
Sample U-C30
Average hydraulic gradient, i_a
Time, t (min)
(b)
Axial compressive strain, ϵ_a (%)
Onset of elastic shakedown
Onset of suffusion

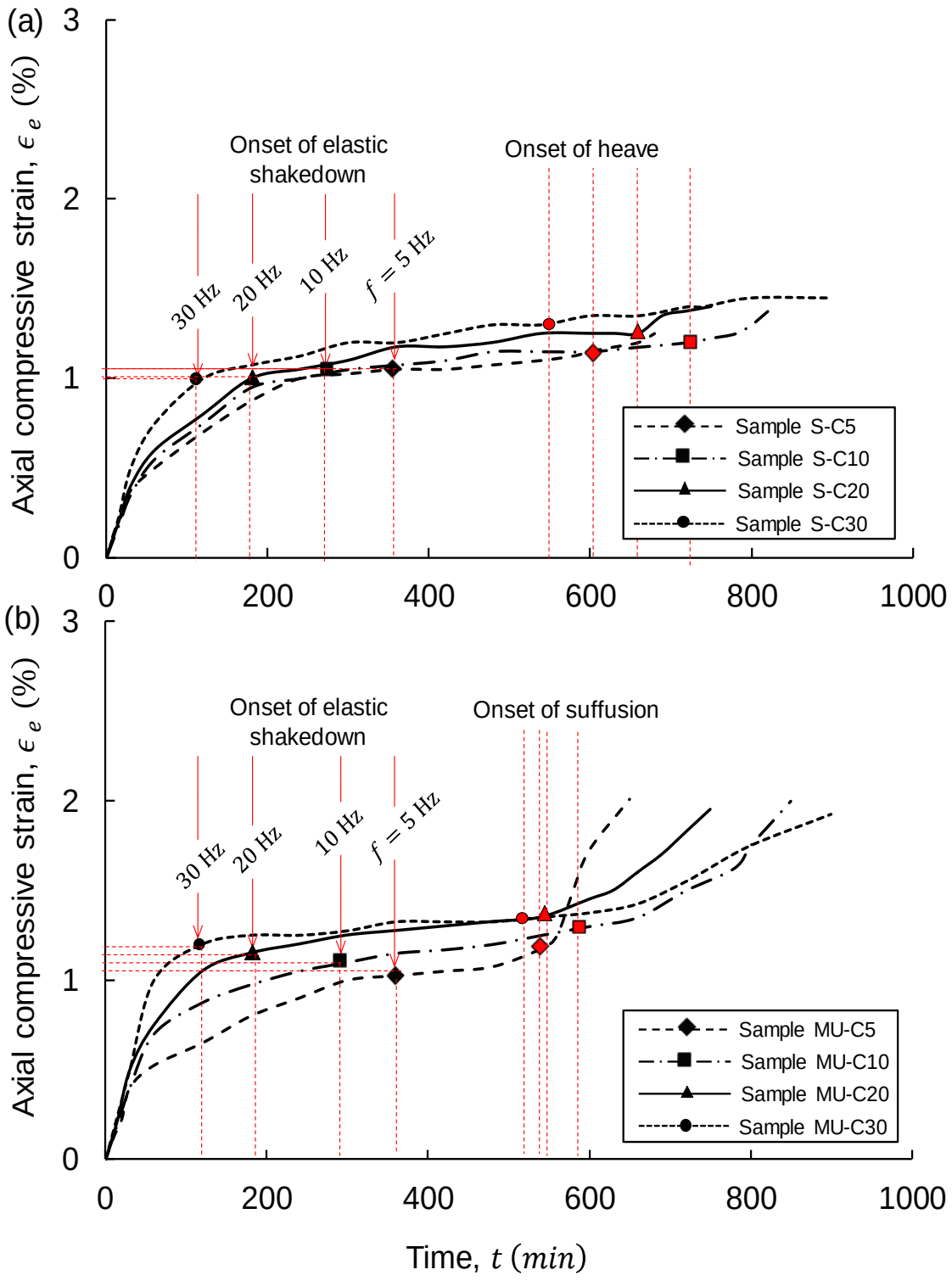
(a)
Axial compressive strain, ϵ_e (%)
Onset of elastic shakedown
Onset of heave
30 Hz
20 Hz
10 Hz
$f = 5$ Hz
Sample S-C5
Sample S-C10
Sample S-C20
Sample S-C30
0
1
2
3
0
200
400
600
800
1000
(b)
Axial compressive strain, ϵ_e (%)
Onset of elastic shakedown
Onset of suffusion
30 Hz
20 Hz
10 Hz
$f = 5$ Hz
Sample MU-C5
Sample MU-C10
Sample MU-C20
Sample MU-C30
Time, t (min)

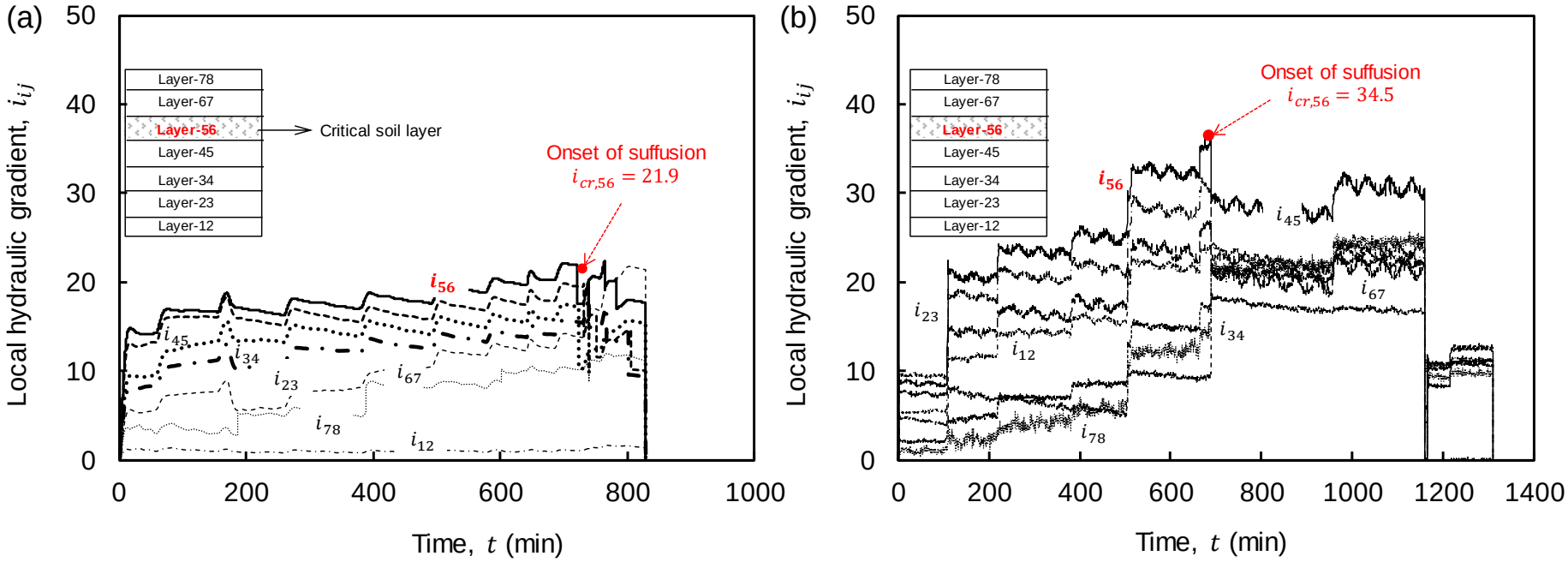
(a)
Local hydraulic gradient, i_{ij}
Time, t (min)
Layer-78
Layer-67
Layer-56
Layer-45
Layer-34
Layer-23
Layer-12
Critical soil layer
Onset of suffusion
$i_{cr,56} = 21.9$
i_{56}
i_{45}
i_{34}
i_{23}
i_{67}
i_{78}
i_{12}
(b)
Local hydraulic gradient, i_{ij}
Time, t (min)
Layer-78
Layer-67
Layer-56
Layer-45
Layer-34
Layer-23
Layer-12
Onset of suffusion
$i_{cr,56} = 34.5$
i_{56}
i_{45}
i_{67}
i_{23}
i_{34}
i_{12}
i_{78}

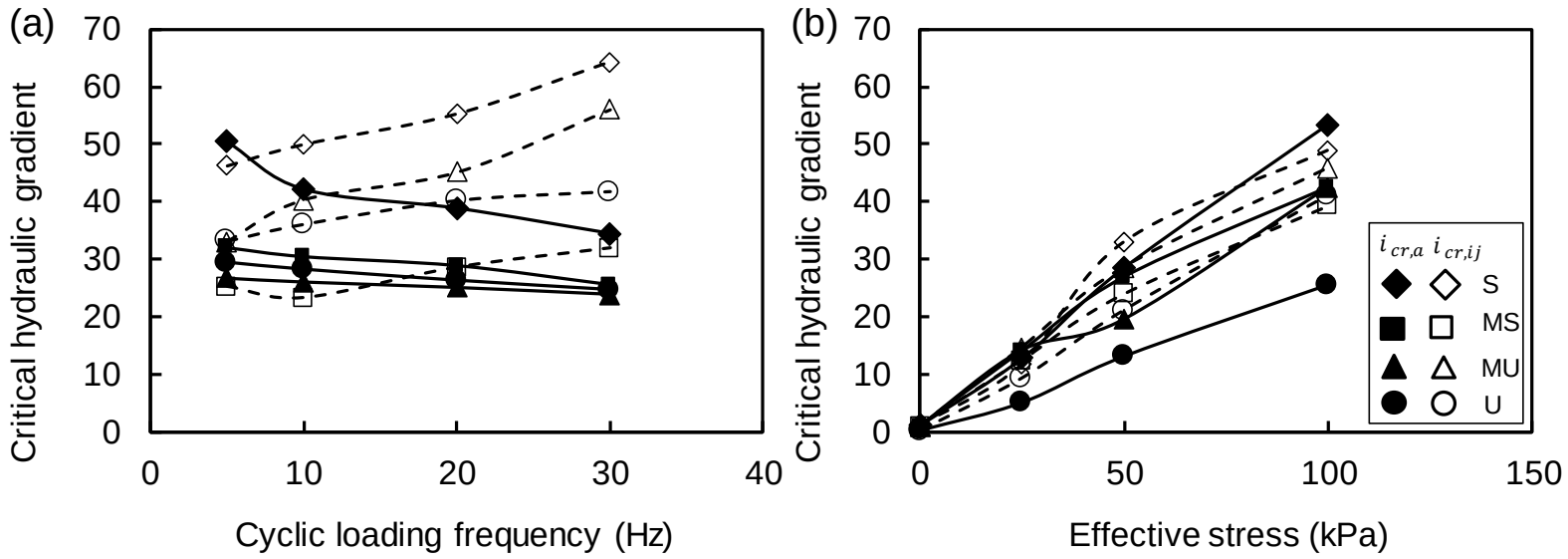
(a)
Critical hydraulic gradient
0
10
20
30
40
50
60
70
0
10
20
30
40
Cyclic loading frequency (Hz)
(b)
Critical hydraulic gradient
0
10
20
30
40
50
60
70
0
50
100
150
Effective stress (kPa)
$i_{cr,a}$ $i_{cr,ij}$
S
MS
MU
U

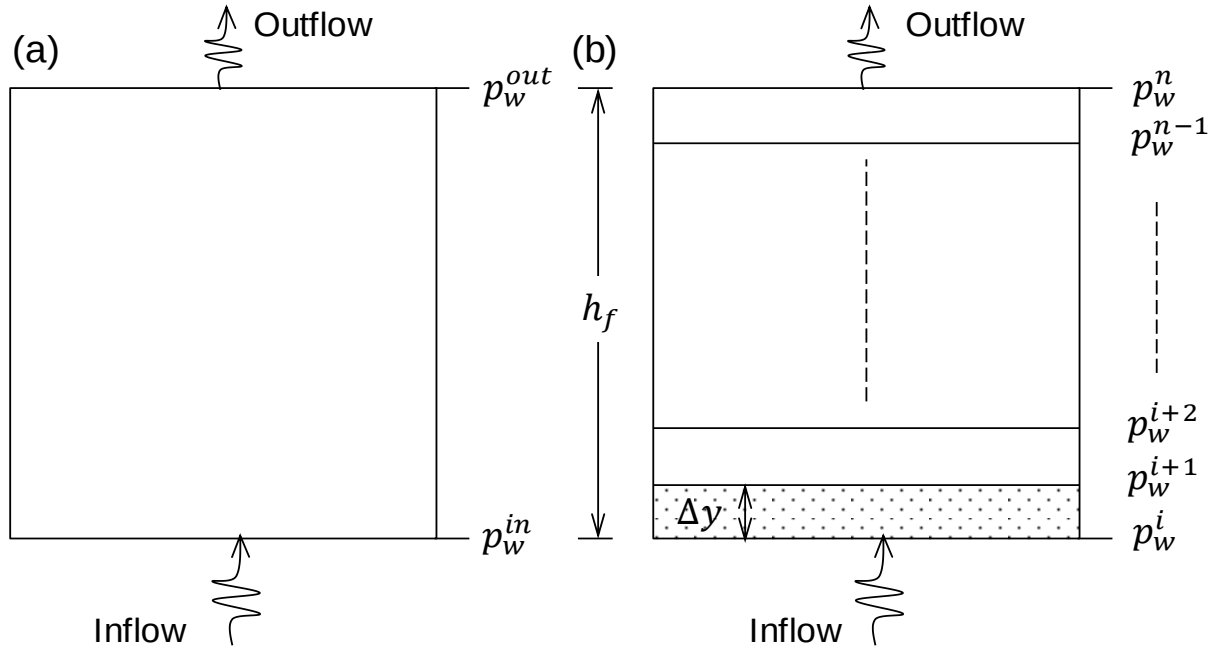
(a)
Outflow
p_w^{out}
p_w^{in}
Inflow
(b)
Outflow
p_w^n
p_w^{n-1}
h_f
p_w^{i+2}
p_w^{i+1}
Δy
p_w^i
Inflow

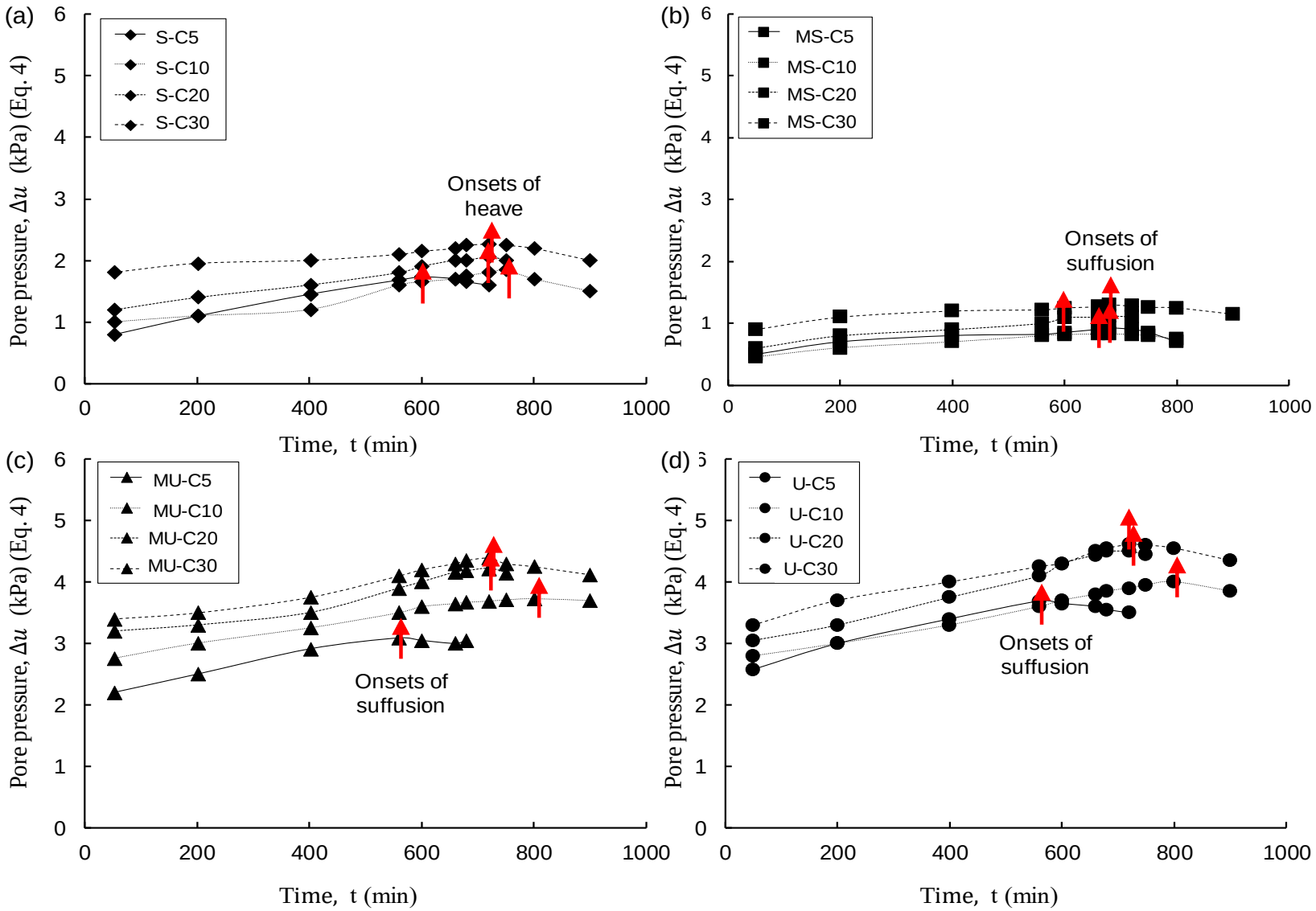
(a)
S-C5
S-C10
S-C20
S-C30
Onsets of heave
Pore pressure, Δu (kPa) (Eq. 4)
Time, t (min)
(b)
MS-C5
MS-C10
MS-C20
MS-C30
Onsets of suffusion
Pore pressure, Δu (kPa) (Eq. 4)
Time, t (min)
(c)
MU-C5
MU-C10
MU-C20
MU-C30
Onsets of suffusion
Pore pressure, Δu (kPa) (Eq. 4)
Time, t (min)
(d)
U-C5
U-C10
U-C20
U-C30
Onsets of suffusion
Pore pressure, Δu (kPa) (Eq. 4)
Time, t (min)

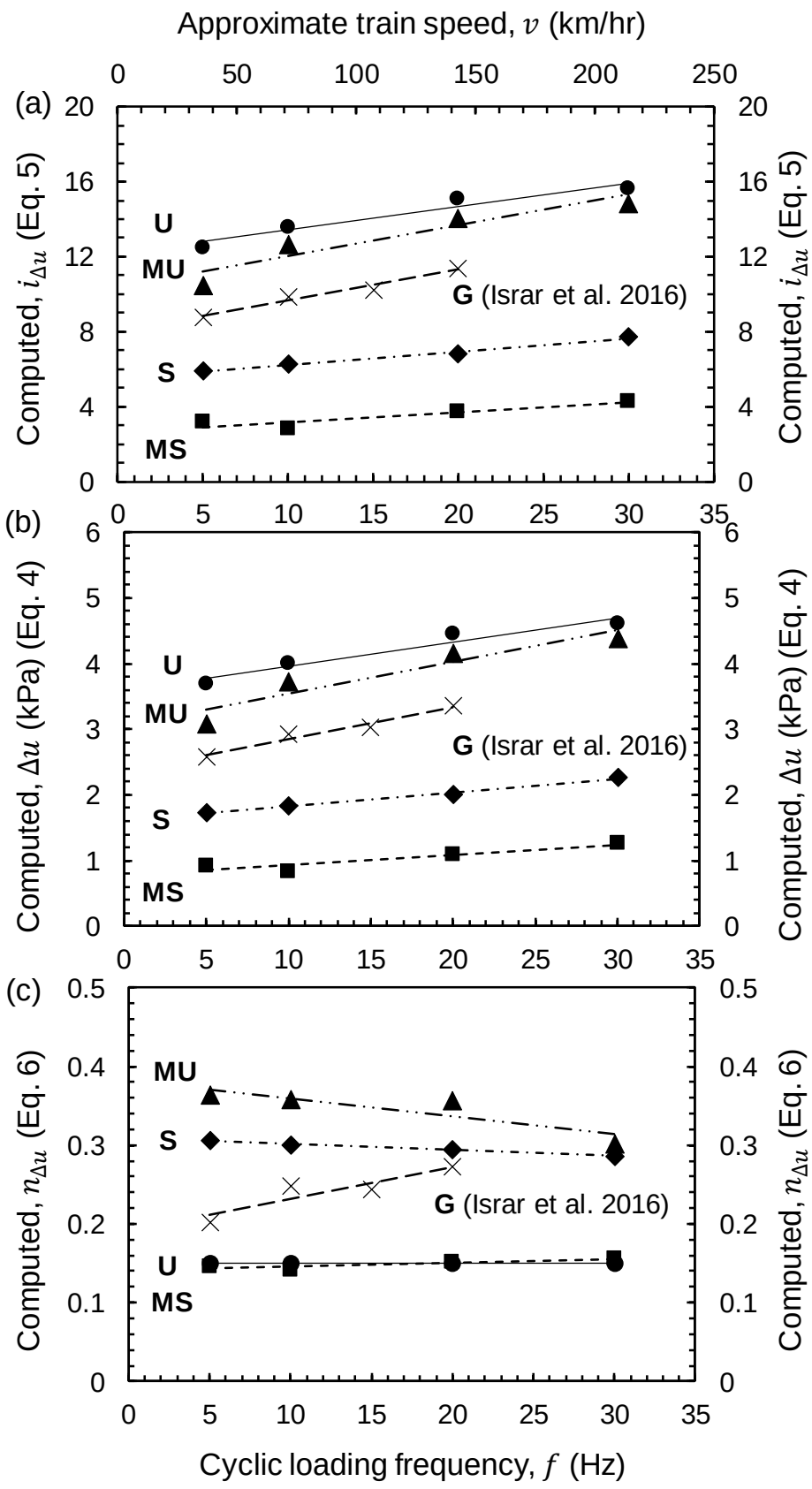
Approximate train speed, v (km/hr)
(a)
(b)
(c)
Computed, $i_{\Delta u}$ (Eq. 5)
Computed, Δu (kPa) (Eq. 4)
Computed, $n_{\Delta u}$ (Eq. 6)
U
MU
S
MS
G (Israr et al. 2016)
Cyclic loading frequency, f (Hz)

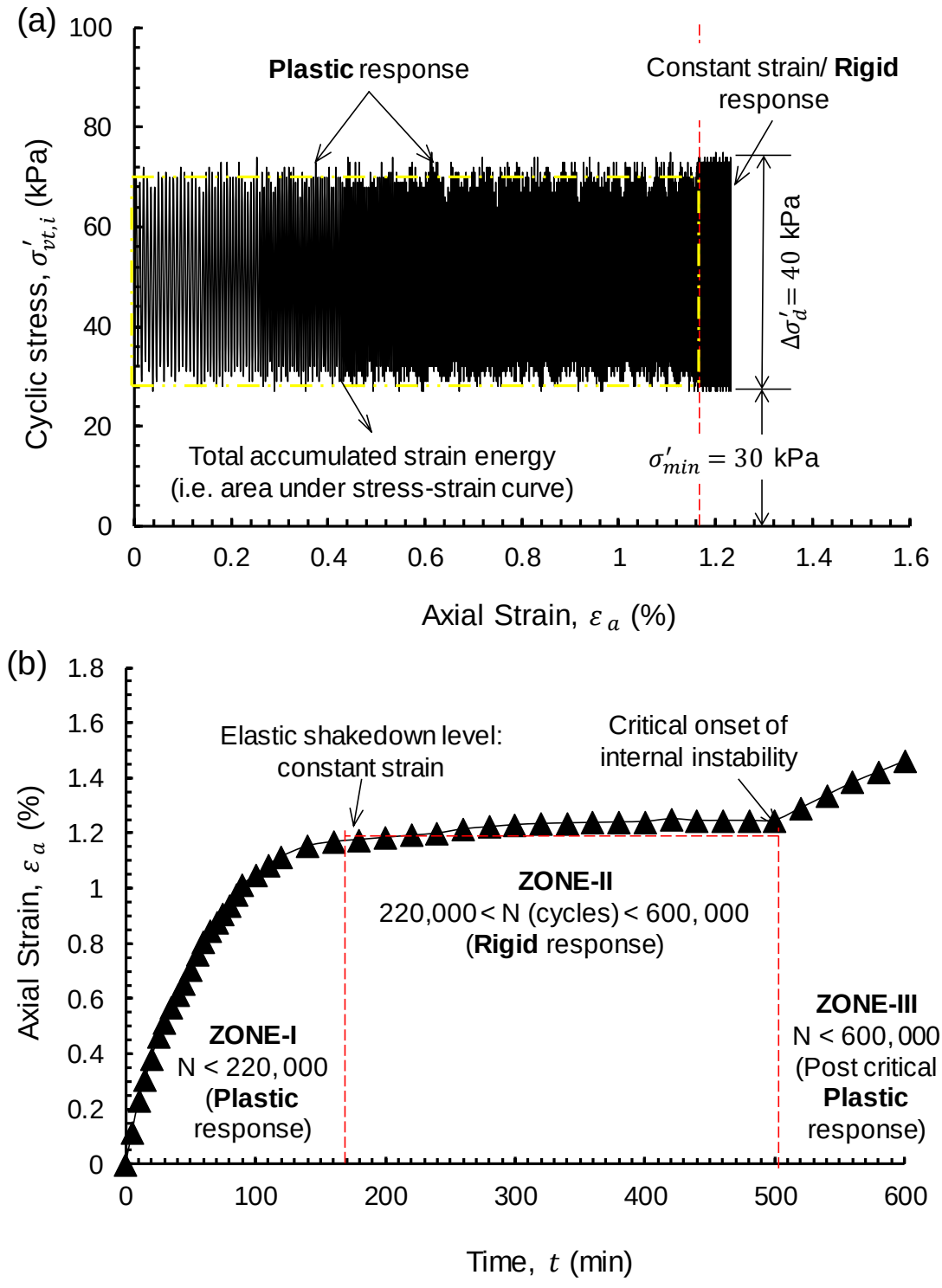
(a)
Plastic response
Constant strain/ Rigid response
Cyclic stress, $\sigma'_{vt,i}$ (kPa)
$\Delta\sigma'_d = 40$ kPa
Total accumulated strain energy
(i.e. area under stress-strain curve)
$\sigma'_{min} = 30$ kPa
Axial Strain, ε_a (%)
(b)
Elastic shakedown level: constant strain
Critical onset of internal instability
ZONE-I
N < 220,000
(Plastic response)
ZONE-II
220,000 < N (cycles) < 600,000
(Rigid response)
ZONE-III
N < 600,000
(Post critical Plastic response)
Axial Strain, ε_a (%)
Time, t (min)

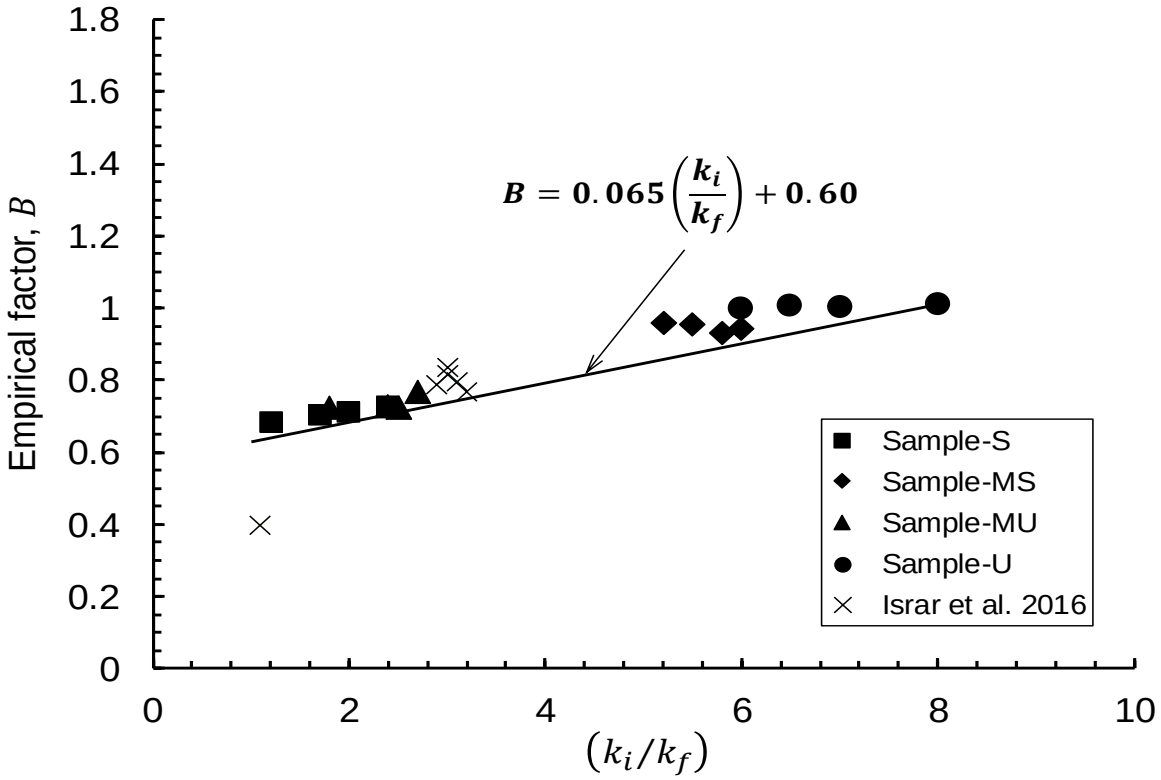
Empirical factor, B
$B = 0.065\left(\frac{k_i}{k_f}\right) + 0.60$
Sample-S
Sample-MS
Sample-MU
Sample-U
Israr et al. 2016
(k_i/k_f)
0
0.2
0.4
0.6
0.8
1
1.2
1.4
1.6
1.8
0
2
4
6
8
10

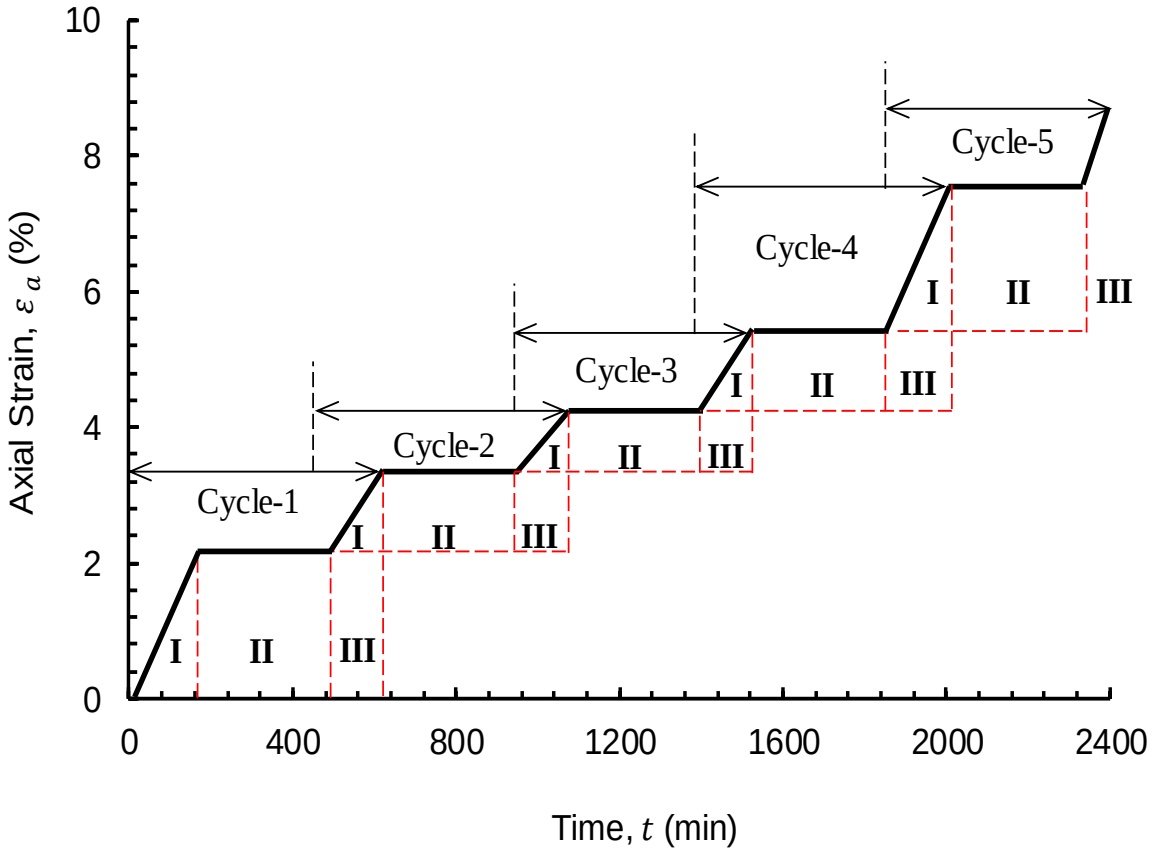
Axial Strain, ε_a (%)
Time, t (min)
0
2
4
6
8
10
0
400
800
1200
1600
2000
2400
Cycle-1
Cycle-2
Cycle-3
Cycle-4
Cycle-5
I
II
III

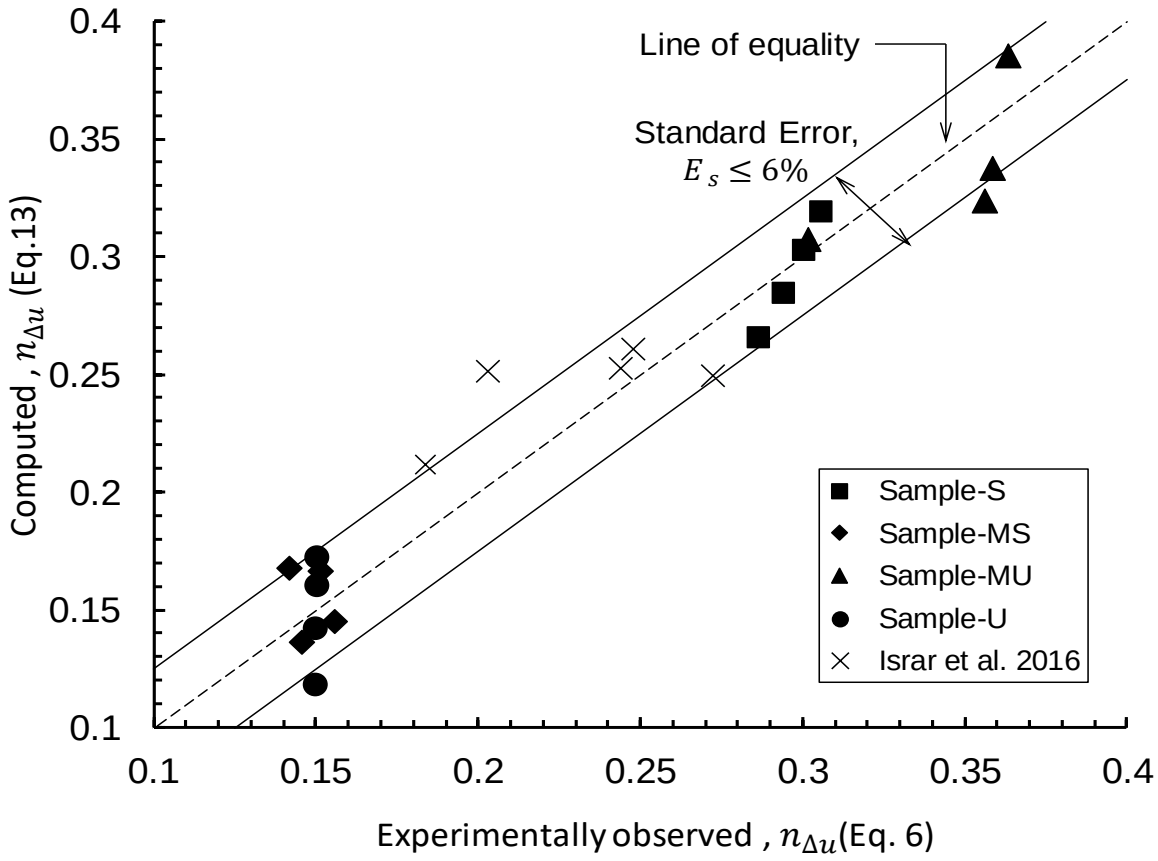
Line of equality
Standard Error,
$E_s \leq 6\%$
Sample-S
Sample-MS
Sample-MU
Sample-U
Israr et al. 2016
Computed , $n_{\Delta u}$ (Eq.13)
Experimentally observed , $n_{\Delta u}$(Eq. 6)
0.1
0.15
0.2
0.25
0.3
0.35
0.4

Table 1. Summary of laboratory test results of this study

Test no.	Sample ID	Relative density (%)		$i_{cr,a}$	$i_{cr,ij}$	$i_{\Delta u}$	Permeability ($\times 10^{-2}$ m/s)		Internal erosion (%)	Post-test Settlement (%)	Failure	Test condition
		Pre-test	Post-test				k_i	k_f				
1	S-S0	96	96	1.14	1.19	--	2.04	2.04	0.03	0.85	Heave	Static loading
2	S-S25	96	96	12.8	12.8	--	1.94	1.94	0.03	1.04	Heave	
3	S-S50	97	97.2	28.5	35.6	--	1.77	1.72	0.02	0.71	Heave	
4	S-S100	96	97	53.4	52.7	--	1.54	1.47	0.01	0.93	Heave	
5	MS-S0	97	97	1.06	1.03	--	1.36	1.36	2.53	0.8	Heave	
6	MS-S25	98	98	14.1	12.8	--	1.24	1.24	2.32	1.13	Heave	
7	MS-S-50	97	97.2	26.9	24.6	--	1.17	1.11	1.71	1.11	Heave	
8	MS-S100	96	96.3	42.5	40.3	--	1.02	1	1.22	1.12	Heave	
9	MU-S0	98	98	0.94	0.98	--	1.27	1.27	3.71	0.99	Heave	
10	MU-S25	98	98	14.1	15.2	--	1.19	1.19	3.05	1.06	Heave	
11	MU-S50	96	96.2	19.5	29.6	--	1.13	1.11	2.83	1.11	Heave	
12	MU-S100	95	95.3	42.5	47.4	--	1.09	1.06	2.51	1.06	Heave	
13	U-S0	97	97	0.26	0.23	--	0.04	0.042	7.37	2.01	Suffusion	
14	U-S25	98	98.2	5.1	9.69	--	0.04	0.035	8.33	1.9	Suffusion	
15	U-S50	99	99.2	13.1	21.9	--	0.03	0.026	7.91	1.93	Suffusion	
16	U-S100	98	98.4	25.5	42.6	--	0.01	0.011	8.89	1.93	Suffusion	

17	S-C5	97	100	50.5	49.8	5.9	1.83	1.525	0.22	1.25	Heave	Cyclic loading
18	S-C10	97	100	42.2	53.8	6.3	1.74	1.024	0.19	1.38	Heave	
19	S-C20	96	100	38.9	59.5	6.8	1.70	0.85	0.26	1.4	Heave	
20	S-C30	98	100	34.5	69.2	7.7	1.65	0.69	0.3	1.45	Heave	
21	MS-C5	97	100	32.1	25.9	3.1	0.95	0.164	4.11	1.68	Suffusion	
22	MS-C10	96	100	30.5	23.9	2.8	0.9	0.173	4.33	1.81	Suffusion	
23	MS-C20	97	100	28.9	29.3	3.7	0.86	0.156	4.52	1.93	Suffusion	
24	MS-C30	98	100	25.5	32.7	4.3	0.83	0.138	4.76	2	Suffusion	
25	MU-C5	98	100	26.8	34.2	10.5	1.1	0.611	5.17	2.01	Suffusion	
26	MU-C10	97	100	26.1	41.7	12.7	1.02	0.425	5.49	2	Suffusion	
27	MU-C20	96	100	25.1	46.7	14.1	0.94	0.376	5.73	1.95	Suffusion	
28	MU-C30	98	100	23.85	57.9	14.9	0.88	0.323	5.93	1.93	Suffusion	
29	U-C5	97	100	29.4	34.5	12.5	0.02	0.0035	12.2	2.24	Suffusion	
30	U-C10	98	100	28.2	37.5	13.5	0.02	0.0026	13.6	2.22	Suffusion	
31	U-C20	99	100	26.3	41.7	15.1	0.01	0.0016	14	2.28	Suffusion	
32	U-C30	99	100	24.7	43.3	15.7	0.01	0.0013	14.2	2.33	Suffusion	

Note: Here, ID, $i_{cr,a}$, $i_{cr,ij}$, k_i and k_f represent identifier, average critical hydraulic gradient, local critical hydraulic gradient, pre-test permeability and post-test permeability, respectively.

Table 2. Summary of laboratory test data adopted from Israr et al. (2016) for validation of current model.

Test series no.	Sample ID	Loading frequency, f (Hz)	Relative density (%)		$i_{cr,a}$	$i_{cr,ij}$	$i_{\Delta u}$	Observation
			Pre-test	Post-test				
1	C	0	95	95.2	50.2	52	--	Heave
2	C	0	95	95.3	51.4	55	--	Heave
3	C	5	96	100	49	56.7	4	Heave
4	F	0	97	97.4	44.5	41	--	Heave-Piping
5	F	0	98	98.3	45.8	44	--	Heave-Piping
6	F	5	97	100	42.4	46.5	7	Heave-Piping
7	G	0	97	97.3	15.3	27.5	--	Suffusion
8	G	0	97	97.4	16.3	26	--	Suffusion
9	G	5	97	100	12.8	30	9	Suffusion
10	G	10	98	100	11.8	30.4	10	Suffusion
11	G	15	97	100	11.5	30.3	10.5	Suffusion
12	G	20	97	100	11.2	31	11.5	Suffusion

Table 3. Parameters for model validation.

Test Series no.	Sample ID	f	$\left(\frac{k_i}{k_f}\right)$	Model parameters		Reference
				A (Eq. 7.9)	B (Eq. 7.10)	
1	S-C5	5	1.2	5	0.678	Current study
2	S-C10	10	1.7	5	0.7105	
3	S-C20	20	2	5	0.73	
4	S-C30	30	2.4	5	0.756	
5	MS-C5	5	5.8	5	0.977	
6	MS-C10	10	5.2	5	0.938	
7	MS-C10	20	5.5	5	0.9575	
8	MS-C30	30	6	5	0.99	
9	MU-C5	5	1.8	5	0.717	
10	MU-C10	10	2.4	5	0.756	
11	MU-C20	20	2.5	5	0.7625	
12	MU-C30	30	2.7	5	0.7755	
13	U-C5	5	6	5	0.99	
14	U-C10	10	6.5	5	1.0225	
15	U-C20	20	7	5	1.055	
16	U-C30	30	8	5	1.12	
17	C	5	1.1	5	0.795	Israr et al. (2016)
18	F	5	1.2	5	0.7885	
19	G	5	2.2	5	0.8015	
20	G	10	2.4	5	0.808	
21	G	15	2.6	5	0.6715	
22	G	20	2.8	5	0.795	

Note: Here, f, k_i and k_f represent cyclic loading frequency, pre-test permeability and post-test permeability, respectively.